



Low Temperature Plasma Technology Laboratory

**Evaluation of Langmuir probe ion density
measurement in weakly ionized discharges
using plasma oscillation probes and
microwave interferometry**

John D. Evans, Wade Zawalski*, and Francis F. Chen
**Hiden Analytical, Ltd.*

LTP-111

November, 2001



Electrical Engineering Department
Los Angeles, CA 90095-1594

Evaluation of Langmuir probe ion density measurement in weakly ionized discharges using plasma oscillation probes and microwave interferometry

John D. Evans^{†1}, Wade Zawalski^{‡2,3}, and Francis F. Chen^{†4}

† UCLA Department of Electrical Engineering,
56-125B Engr. IV, UCLA 159410
Los Angeles, California, 90095 USA

‡ Hiden Analytical, Ltd.
420 Europa Boulevard, Warrington, WA5 7UN UK

(Short title: *"Evaluation of Langmuir probe N_i measurement via POP and MWI"*)

(PACS #s in order of relevance;)

(52.70.-m, 52.70.Ds, 52.70.Gw, 52.50.Qt, 52.80.Pi, 52.50.Dg)

¹ jdevans@ucla.edu

² Presently at IMEC, Kapeldreef 75, B-3001 Leuven, Belgium

³ wade_zawalski@imec.be

⁴ ffchen@ee.ucla.edu

ABSTRACT

A comparison study is made of the classical theories of the determination of the ion density N_i from the ion current I_i to a cylindrical Langmuir probe vs bias voltage V_b in weakly ionized RF plasmas. A broad parameter range is examined in a commercial inductively coupled plasma (ICP). Accurate local electron density N_e values ($N_{e,MWI}$) obtained from Abel inversion of chord-averaged microwave interferometry (MWI) measurements using radial profiles $N_i(R)$ from Langmuir probes, are verified by comparison with N_e from a plasma oscillation probe, and then compared with N_i obtained from theoretical interpretations of the probe current $I_p(V_b)$ characteristics using a Hiden[®] Langmuir probe. Observed agreement between $N_{e,MWI}$ and N_i thus obtained ranges from poor to fair; best agreement is observed at low pressure and RF power. A heuristic alternative approach based upon the Child-Langmuir law of ion sheath expansion ($I_i \propto V_b^{3/4}$) is described, whereby N_i is determined by extrapolation of a linear regression fit to I_p , in the ion saturation regime, to its value $I_i(V_f)$ at $V_b = V_f$, the floating potential. Good to excellent agreement with $N_{e,MWI}$ is thus obtained, far superior to that using conventional analyses, despite the nonrigorous foundation for this “floating potential” method.

1. Introduction

Proper theoretical evaluation of the ion density N_i from the current-voltage characteristics (I - V curves) of a Langmuir probe [2] has been a subject of ongoing controversy [3-7] since the inception of the Orbital Motion Limited (OML) theory in the pioneering work of Mott-Smith and Langmuir [8]. More modern treatments include the Allen-Boyd-Reynolds (ABR) radial motion theory [3] and the Bernstein-Rabinowitz theory [4] for the monoenergetic ion case, as extended by Laframboise [7] to treat the ion flux I_i to a cylindrical probe tip in a Maxwellian plasma. ABR assumes that ions have zero initial velocity, hence zero (conserved) angular momenta L_m about the probe tip of radius R_p , at a distance $R \rightarrow \infty$, so that all ions accelerate radially towards the probe and are thus eventually collected. If one hypothesizes an "absorption region" as the locus of points that lie within a boundary of average distance R_a surrounding the probe tip, such that only those ions that cross the boundary are collected by the tip, it is clear that in ABR theory $R_a \rightarrow \infty$ encompasses the entire plasma.

In contrast, the orbital motion model (figure 1) permits finite ion temperature T_i , and thus finite L_m . Ions with sufficient L_m follow open orbits ($R > R_a$) that miss the probe, whereas the others traverse closed trajectories and are collected. Note, however, that $L_m \rightarrow \infty$ as $R \rightarrow \infty$ for finite temperature ions, which appears to be unphysical unless $T_i = 0$ at infinity; conservation of L_m ($= 0$) would then imply that the ion motion is purely radial for ions coming in from infinity, which is exactly the premise of the competing ABR theory and inconsistent with the initial assumptions of the orbital motion model. OML is a special case where no absorption radius exists, valid in the "thick sheath" regime (here, $N_e \equiv$ electron density, $T_e \equiv$ electron temperature, and $\lambda_D \equiv [\epsilon_0 T_e / e N_e]^{1/2}$ is the Debye length):

$$\xi_p \equiv R_p / \lambda_D \leq 3. \quad (1.1)$$

Clearly, neither ABR nor OML constitutes a complete theory. However, the Bernstein-Rabinowitz formulation as extended by Laframboise (BRL) is complete in that it permits finite T_i and also treats the $T_i \rightarrow 0$ case in cylindrical geometry, thus being potentially applicable in virtually all collisionless plasmas. Early studies by Chen *et al* [5] established that the theoretically sound BRL approach yields N_i values in good agreement with N_e obtained from microwave interferometry (MWI) measurements in a fully ionized Q-machine. Such findings would normally lead to acceptance of BRL as the theory of choice over OML and ABR, except that BRL overestimates N_i in the weakly ionized RF plasmas of current interest [9], probably because such plasmas are not truly collisionless. In a typical processing plasma, the neutral pressure P_0 , and thus neutral density N_0 and the ion-neutral collision frequency ν_{i0} , are large enough to significantly perturb the (otherwise collisionless) trajectories of ions in the vicinity of the probe; collisionality therefore leads to an enhancement of I_i over its BRL theoretical value and therefore to an overestimation of N_i .

Despite its apparent shortcomings, OML is attractive in that it yields a simple formula for I_i to a cylindrical tip of length L_p in terms of $V_0 \equiv - (V_b - V_s)$, where $V_b \equiv$ probe bias voltage and $V_s \equiv$ plasma potential, in the ion saturation regime ($V_0 \gg T_e$):

$$I_i \xrightarrow{T_i \rightarrow 0} = e A_p N_i \frac{\sqrt{2}}{\pi} \left(\frac{V_0}{M_i} \right)^{1/2}, \quad (1.2)$$

where $A_p \equiv 2\pi L_p R_p$ is the tip area and $M_i \equiv$ ion mass. Equation (1.2) is independent of T_e and easy to use; the slope of a least squares fit of I_i vs $V_0^{1/2}$ is proportional to N_i for a given V_s . This latter quantity is often determinable from the electron retardation region of the I - V curve ($T_e \lesssim V_b \lesssim V_s$), and thus N_i is obtained.

In practice, it is often found that I_i appears to vary as $V_0^{1/2}$ at low densities. However, it is known that ABR [10] and BRL [11] also exhibit $I_i \propto V_0^{1/2}$ behavior in the thick sheath regime. Confusion may therefore arise as to whether an observed agreement between probe data and an I_i vs $V_0^{1/2}$ least squares fit constitutes experimental verification of BRL, OML, or ABR, even though BRL is the most theoretically sound. If OML is blindly applied anyway, it is often observed that the intercept of the I_i^2 vs V_0 least squares fit yields a value of V_s [at $I_i(V_s) = 0$, from equation (1.2)] very different from the accurate result using the widely accepted Druyvestyn [13] method. Finally, order of magnitude discrepancies between probe-determined N_i values and N_e results obtained using other methods are reported [14,15] in low-density plasmas, for which equation (1.2) is expected to apply.

At the other extreme, $\xi_p \gg 1$ (“thin sheath” approximation), BRL reduces to

$$I_i \cong 0.4eN_i A_p u_B \quad (1.3)$$

where $u_B \equiv (eT_e/M_i)^{1/2}$ is the Bohm velocity. Equation (1.3) differs from the Bohm result only in the leading coefficient: values $\sim 0.4 - 0.6$ appear in the literature. An apparent feature of equation (1.3) is the lack of dependence upon V_0 , such that the probe current I_p approaches this value as $V_0 \rightarrow \infty$, implying that its validity can be checked by adjusting V_0 and verifying that I_i indeed remains constant. Although this condition is often met in high- N_p plasmas such as helicon discharges ($N_e \geq 10^{12} \text{ cm}^{-3}$), it does not hold for all of the parameter regimes of an ICP, particularly at low RF power. Again, the experimentalist is denied a simple, reliable theory for N_i from I - V curves.

A renewed interest in the proper interpretation of I_i vs V_0 , and the need for reliable *in situ* plasma diagnostics in general, has arisen with the ongoing growth in popularity of weakly ionized RF discharges [16,17] in the plasma processing industry. A wide variety of RF plasma production schemes are employed, each posing its own challenges in regards to the measurement of plasma parameters. In particular, RF-induced V_s fluctuations can distort Langmuir probe characteristics, leading to an overestimation of T_e [17] and N_i [11,18]. Nevertheless, RF distortion of I_i is expected to be less severe than that of the electron current I_e , so it appears worthwhile to demonstrate the reliable determination of N_i from I_i in a weakly ionized RF plasma by using an independent diagnostic method to determine N_p , and comparing these results.

Despite the need for such a demonstration, surprisingly few accounts of such research appear. An earnest attempt was made by Tuszewski and Tobin [11] using spatially averaged $\langle N_e \rangle$ from MWI to compare with the local N_i from a Langmuir probe in a variety of plasma processing relevant gases. Indeed, it was shown that RF distortion leads to an overestimation of N_i (~ 2 - 3 x), obtained using BRL. However, the validity of the technique used for comparison of $\langle N_e \rangle$ with the local $N_i(0)$ probe value was not established, and thus the accuracy of BRL was left undetermined.

In the present work, we present the results of a comprehensive comparison study, in a commercial ICP reactor, of central $N_i(0)$ measurements obtained by applying the above classical probe theories to the I - V curves from a cylindrical Langmuir probe, with (a) the local $N_e(0)$ using the plasma oscillation probe (POP) method, and (b) the spatially-averaged $\langle N_e \rangle$ from MWI. The connection between the nonlocal MWI values ($\langle N_e \rangle_{MWI}$) and the local $N_i(0)$ probe measurement is established by Abel inversion; the profile normalization factor $F_{norm}(0) \equiv N_p(0)/\langle N_p \rangle$ is obtained from *relative* (not *absolute*) values of $N_p(0)$ and $N_p(R)$ using a radially scannable Langmuir probe, and then used to solve for $N_e(0)$ from the chord-averaged $\langle N_e \rangle_{MWI}$ value. This partially inferred $N_e(0)$ is compared to the POP result as an independent check of the Abel inversion. If satisfactory agreement is obtained, a comparison is then made with $N_i(0)$ from the I-V curve using the various probe theories, as well as with the electron density $N_{e,Ies}(0)$ obtained from the electron saturation current $I_{es} \equiv I_p(V_s)$. The results are used to choose the appropriate theory of ion current collection in weakly ionized RF plasmas.

Surprisingly, it is found that a heuristic approach based on the Child-Langmuir law of ion sheath expansion, whereby it is *postulated* that $I_i \propto V_0^{3/4}$, and a least squares fit to the I_i data yields N_i values that exhibit better agreement with $N_{e,MWI}$ than the classical probe theories throughout the range of parameters studied here. Extrapolation of said fit to its value at the floating potential V_f yields $I_i(V_f)$, which together with the Bohm criterion, provides an analytical solution for N_i as a function of V_s and T_e . This "floating potential method" is successful despite its apparent lack of rigor.

2. Experimental Apparatus and Diagnostic Methods

The experimental device shown in figure 3 consists of a PlasmaTherm[®] ICP source module, mounted on top of a "magnetic bucket" [19] vacuum chamber that is lined with an array of permanent magnets (not shown), arranged in vertical columns in alternate line cusp configuration. Such an edge-localized magnetic confinement scheme significantly enhances the plasma density (N_p) uniformity, especially near the edge [20], as well as increases the overall density. Edge uniformity is particularly desirable, as it dramatically decreases the discrepancy between the chord-averaged density $\langle N_p \rangle$ and the local $N_p(0)$ central value. Several neutral gas feed ports are used, one near the top and two diametrically opposite each other near the bottom (not shown), to minimize azimuthal asymmetry. It proved necessary to cool the tube (with a fan in this case) connecting the plasma chamber to the neutral pressure (P_θ) gauge, and thus keep the neutrals sampled therein near room temperature, so as to permit the determination of the neutral gas density (N_θ) from the P_θ measurement. An RFPP[®] RF10M generator with built-in automatic impedance matching network is used to couple RF power $P_{rf} \leq 1\text{kW}$ at fixed frequency $f_{RF} = 2\text{MHz}$ into the spiral-shaped antenna element within the ICP module. This antenna encircles a ~ 1 cm thick insulating ceramic liner which comprises the antenna-plasma boundary. Plasma is produced and sustained at 5 power levels (300-900W at 150W intervals) and 4 neutral pressures (1, 2, 5 & 10 mTorr), thereby forming a 20-element experimental matrix that spans a wide range of operating parameters of interest to the processing industry. Experiments are performed in the collisional regime; the ratio of the electron collision frequency (f_{coll}) to RF frequency $f_{coll}/f_{RF} \gtrsim 1$ is such that Ohmic resistive dissipation is predicted to dominate.

Figure 4 shows a detailed conceptual diagram of the essential elements of each diagnostic. MWI consists mainly of an HP 8510C network analyzer, which both launches and mixes the signal and reference legs while sweeping the frequency $f_{\mu w}$. The phase shift $\Delta\Phi$ between the two legs versus $f_{\mu w}$ is thereby obtained, yielding accurate values of the line-averaged density $\langle N_e \rangle$ vs $f_{\mu w}$ along a chord that intersects the region ($R \sim 0$, axial distance $z \sim 22\text{cm}$ below top plate) sampled by the POP and Langmuir probe. The POP consists of an antenna in close ($\sim 1\text{ cm}$) proximity to a filament, biased in such a way that a beam-plasma instability, at oscillation frequency f_{osc} approximately equal to the electron plasma oscillation frequency $f_{pe}(0)$, is excited near the filament and detected by the antenna. This signal is fed into a spectrum analyzer, thereby yielding an independent measurement of $N_e(0) \propto \sqrt{f_{pe}(0)}$. The resultant $N_{e(0),POP}$ is then compared to the MWI value $N_{e(0),MWI}$ obtained from Abel inversion of $\langle N_e \rangle_{MWI}$ using $N_i(R)$ from a radially scanable Langmuir probe, as a check of the validity of this MWI technique. If satisfactory agreement is observed, then $N_{e(0),MWI}$ is treated as the true $N_e(0)$ value, which is used as the basis for comparison with $N_i(0)$ from the Langmuir probe using the various probe theories to determine which theory yields the most accurate results in weakly ionized RF plasmas.

2.1. Langmuir Probe (LP)

Figure 5 shows a schematic of the commercial Hiden[®] [1] Langmuir probe (ESP[™]) used for all Langmuir probe measurements. RF distortion of the I - V curve is reduced by a choke located within the shaft near the tip and a large compensation electrode that is capacitively coupled to the tip, in order to drive it at the RF frequency and thus track $V_s(t)$. Hiden uses a standard tip size, $R_p = 0.075\text{ mm}$ and $L_p = 1\text{ cm} \gg R_p$, to facilitate the use of cylindrical probe theory, and so the criterion for validity of OML (equation 1.1) is satisfied in many cases. Let X_{sh} be the thickness of the sheath surrounding the tip; R_p is such that R_p/X_{sh} goes through unity within the range of parameters spanned by the experimental matrix. A Hiden Hal IV[™] probe driver interface unit (Fig. 4) was used to simultaneously sweep V_b and measure I_p in order to obtain high quality I - V curves. Hal IV is operated from a PC programmable interface using the ESPsoft[™] Langmuir probe data acquisition/analysis software package, which is user friendly and allows for rapid data analysis. Figure 6 is a typical I - V curve, which forms the basis of the ESPsoft analysis example outlined below.

Semi-automatic data analysis proceeds as follows. Taking the first derivative of the I - V curve and finding its maximum value (equivalent to setting $d^2I/dV^2 = 0$) according to the Druyvestyn approach [13] yields $V_s \cong 14.2\text{V}$ (figure 7). Next, I_p^2 vs V_b is generated, and the user adjusts the scale until it looks similar to figure 8. Ion current analysis is then performed manually in conjunction with the ESPsoft OML algorithm, which calculates a least squares fit ($I_{ion-fit}$) of a user-selected interval of the curve, similar to the red dashed line of figure 8. From equation (1.2), it is seen that OML theory requires that the extrapolation of $I_{ion-fit}$ intersects the V_b -axis at V_s . However, in practice a compromise is made between the quality of the fit, the range over which the fit is obtained, and the degree to which this $I_{ion-fit}(V_s) = 0$ constraint is met. In many cases, a linear regression fit over the entire ion saturation region will not extrapolate to $I_{ion-fit}(V_s) = 0$, as it should according to equation (1.2). Usually, however, a fit can be found that satisfies this condition, but this fit is of good quality over only a limited portion of the I - V curve in the near-ion saturation current region. In the case of figure

8, the interval $-50\text{V} < V_b < -7.2\text{V}$ was selected, yielding an $I_{ion-fit}$ (red dashed line) with V_b -intercept = $14\text{V} \cong 14.2\text{V} = V_s$, in approximate agreement with that obtained using the Druyvestyn method. However, (see Introduction) a good $I_p^2 \propto V_b$ fit does not in itself constitute proof of the validity of OML. Assuming for the moment that OML does indeed apply, equation (1.2) yields $N_{i,OML}$ from $I_{ion-fit}$. Analysis proceeds by taking the square root of $I_{ion-fit}^2$ and subtracting the resulting $I_{ion-fit}$ from the source curve I_p , yielding an approximation to the electron current component $I_e \cong I_p - I_i$ of the original $I-V$ curve. Taking $\text{Ln}(I_e)$ and choosing a linear regression fitting interval, we obtain the slope = $1/T_e$. ESPsoft then calculates N_e from the electron saturation current $I_{es} = eA_p N_e (KT_e/2\pi m)^{1/2}$ using T_e and V_s from above, and displays the results in tabular form (Table 1) along with fitting parameters (note: the substitutions " V_p " \rightarrow V_s , " N_i +" \rightarrow $N_{i,OML}$ and " Ne " \rightarrow $N_{e,Ies}$ are used henceforth). All I-V curves, and their associated $N_{i,OML}$ and $N_{e,Ies}$ values, were obtained in this fashion. Radial profiles were also obtained, at $z = 22$ cm, for calibration of the MWI results (Section 2.2).

Parameter	Value	Units	Degree of accuracy: <i>Comments by authors</i>
Position	0	cm	<i>n/a</i>
Time	42.4	seconds	<i>n/a</i>
Vf	2.24	V	
Vp Est.	14.2	V	<i>From Druyvestyn method</i>
Vp	14.26	V	<i>From intersection of M1 & M2: Used for I_{es}</i>
I(Vp)	0.037	Amps	<i>Evaluated at $V_b = "Vp Est."$</i>
I(Vp)data	0.038	Amps	<i>Evaluated at "V_p": Used for I_{es} to calculate "Ne"</i>
Te	3.13E+04	K	
Te	2.69E+00	eV	<i>From user defined fit: slope="M1 Gradient"=$1/T_e$</i>
Ne	1.80E+17	/m3	<i>From T_e & I_{es} : => $N_{e,Ies}$</i>
Ni+	3.59E+17	/m3	<i>From user selected "IC Gradient": => $N_{i,OML}$</i>
Db	2.88E-05	m	<i>Debye length λ_D</i>
Area	4.7	mm2	<i>Cylindrical probe tip area $A_p \cong 2\pi R_p L_p$</i>
IC V Start	-50.1	V	<i>Linear regression interval - I_p^2 vs V_b : begin</i>
IC V End	-7.2	V	<i>" " " " : end of regression fit interval</i>
IC Gradient	-3.53E-08	+/-	$1.57\text{E}-10$: Yields $N_{i,OML}$ from Eqn (1.2)
IC Intercept	4.84E-07	+/-	$4.50\text{E}-09$: Yields $V_s = (-intercept/gradients)$
IC # points	430		
M1 V Start	0	V	<i>Linear regression interval - $\text{Ln}(I_e)$ vs V_b : begin</i>
M1 V End	10	V	<i>" " " " : end of regression fit interval</i>
M1 VMaxSlope	0	V	
M1 Gradient	0.3711	+/-	0.001444 : T_e (eV) = $1/(M1 Gradient)$

M1 Intercept	-8.216	+/-	0.007222 : <i>Intersection of M1 & M2 lines=>V_p</i>
M1 # points	101		
M2 V Start	17.6	V	<i>Linear regression interval-Ln(I_{es}) vs V_b : begin</i>
M2 V End	24.8	V	<i>" " " " : end of regression fit interval</i>
M2 Gradient	0.05145	+/-	0.000463
M2 Intercept	-3.659	+/-	0.009825 : <i>Intersection of M1 & M2 lines => V_p</i>
M2 # points	73		

Table 1: ESPsoft "Full Report", tabulated results obtained with the Langmuir probe, along with authors' comments in *italics*. Notation substitution: " V_p " \rightarrow V_s , " N_i +" \rightarrow $N_{i,OML}$ and " N_e " \rightarrow $N_{e,Ies}$.

ABR and BRL routines were developed in house [21] and used in Excel™ spreadsheets; ESPsoft I-V curves were imported and analyzed, and the results plotted (figure 10). In this example ($P_0 = 5$ mTorr), neither ABR nor BRL achieved much better than factor-of-two accuracy when compared with the true MWI N_e values [22], whereas OML yields the best overall agreement of the classical probe theories. Indeed, the normalized probe radius varies from $1 \lesssim \xi_p \lesssim 4$ over the sampled parameter range; the OML validity condition (equation 1.1) holds in most cases.

2.2. Microwave Interferometry (MWI)

As indicated in figure 4, microwaves at frequency $f_{\mu w}$ are beamed into the discharge (S_{in}) from a transmitting horn through one window, traverse the plasma and thus undergo phase shifting due to the alteration of the beam phase velocity by the dielectric plasma medium, then exit through a diametrically opposite window (S_{out}) and enter the receiving horn. The phase of this outgoing "signal" beam (Φ_p) is measured (detected) by mixing it with a fixed reference signal. This process is repeated in the absence of plasma, yielding Φ_0 , the vacuum phase value. The measured phase delay $\Delta\Phi = |\Phi_0 - \Phi_p|$ is used to calculate the average electron density $\langle N_e \rangle$ sampled by the signal beam (see below) over its entire path. Basic treatments of MWI are found in Chen [23] and Lieberman [24]; the technique used in the present work is an improved, modern version of this basic scheme. An HP 8510C vector network analyzer replaces the klystron, oscilloscope, attenuator and phase shifter from the classic [23,24] MWI setup. Amplitude and phase $\Delta\Phi$ are measured with resolutions of 0.05 dB and 0.5 degrees, respectively. Also, $f_{\mu w}$ is swept over an interval, so that a plot of $\Delta\Phi$ vs $f_{\mu w}$ is generated. Problematic $f_{\mu w}$ intervals [25] are identified and avoided (see below) by using this technique, whereas they may go undetected in fixed frequency configurations.

Let s denote the position of a point along the path \mathcal{S} of the signal beam. The chord-averaged electron density $\langle N_e \rangle$ along \mathcal{S} is given by:

$$\langle N_e \rangle \equiv \int_{S_{in}}^{S_{out}} N_e(s) ds / \int_{S_{in}}^{S_{out}} ds \equiv (1/S) \int_{S_{in}}^{S_{out}} N_e(s) ds \quad (2.1)$$

It is thus important to choose \mathcal{S} such that its length $S \equiv |S_{out} - S_{in}|$ is easily determined, and thus $\langle N_e \rangle$ readily evaluated. Care must be taken in this regard. Let λ_p (λ_0) be the plasma (free-space) wavelength of the beam. Small-diameter plasma columns, for which the wave number within the plasma $k_p \equiv 2\pi/\lambda_p \sim 2\pi/S$, will diffract the beam and thus cause it to traverse an *a priori* unknown path length - possibly not arriving at the receiving horn at all. Plasma cylinders, a common discharge geometry, can cause significant refraction if the free-space wave number k_0 is comparable to $2\pi/R_c$, where R_c is the local radius of curvature of the plasma boundary. Finite chambers (especially metallic cylinders) can have multiple internal reflections of all or part(s) of the beam, leading to a weighted phase averaging over an unknown mixture of path lengths. The refractive index $\mathcal{N}_p \equiv k_p c/\omega = \lambda_0/\lambda_p$ that determines the phase of the beam as it traverses the plasma is a function of s when N_e gradients are present; such gradients are inevitable in laboratory discharges near the boundaries, although their significance varies. Aperture size, in this case the diameter of the vacuum-chamber interface windows d_w of the beam ports, must be carefully chosen; severe diffraction and internal reflections can occur if $\lambda_0, \lambda_p \sim d_w$.

All of the above-mentioned difficulties can be overcome in practice as follows: (a) choose \mathcal{S} to lie along a central chord such that its path through the plasma is symmetric, in order to minimize possible refractions, (b) select $f_{\mu w}$ such that $\lambda_p \ll a$, where a is the radius of the chamber, so that the plasma edge "looks flat" to the beam and refraction is thus minimized, (c) use microwave-absorbing material on the walls of the chamber--the bucket has anodized walls which do not reflect microwaves particularly well, but this is not relied upon here, (d) do the measurements on a plasma region with a fairly uniform $N_p(R)$ (ICPs are remarkably so) and gentle gradients, if given a choice, and (e) further choose $f_{\mu w}$ such that $f_p^2/f_{\mu w}^2 \leq 0.1$, so that the reflected/absorbed power is an insignificant fraction of the transmitted power [25].

It is also convenient to choose $f_{\mu w}$ such that $\Delta\Phi$ is a significant fraction of, but not greater than, a single fringe (2π); this permits the unambiguous and yet accurate determination of $\Delta\Phi$ in case the plasma initiates too rapidly to permit an accurate count of multiple fringes, even with a fast storage oscilloscope. It is not uncommon for the beam to be severely refracted, or even lost altogether, in a rapidly time-varying plasma with large transient N_e gradients. It is apparent when signal loss occurs, as rapid and erratic discontinuities in $\Delta\Phi$ appear. However, network analyzers are very sensitive, and the signal was never lost during the experiment. Accurate $\Delta\Phi < 2\pi$ measurement is achieved by judicious choice of fixed $f_{\mu w}$ or a swept- $f_{\mu w}$ technique over a suitable range. Amplitude information can be safely ignored as long as it is too small to produce appreciable plasma; it is the phase shift that is of utmost interest.

An additional potential source of error stems from the fact that $\Delta\Phi$ is averaged over all paths that are traversed by the microwaves from their point of entry S_{in} (transmitting horn at near window) to their exit S_{out} (receiving horn at far window). Phase averaging over multiple beam paths leads to a systematic error in the direction of increased $\Delta\Phi$, since all alternate paths are longer than the desired direct signal path \mathcal{S} , leading to an overestimation of N_e if proper care is not taken. Whereas this effect may be difficult to eliminate, or even detect, when a single $f_{\mu w}$ is used, it is readily detected by sweeping over a range of $f_{\mu w}$ and examining the resulting $\Delta\Phi$ vs $f_{\mu w}$ plots. Multiple beam paths are indicated by discontinuities in said

graphs, which are readily avoided by sweeping over a range of $f_{\mu w}$ and choosing an interval for which $\Delta\Phi(f_{\mu w})$ has nearly constant slope (constant N_e). Generally, an interval for which broad local minima in $\langle N_e \rangle \propto \Delta\Phi/f_{\mu w}$ vs $f_{\mu w}$ are observed in the parameter range of interest is desired. Such a well-behaved interval (82-88 GHz) was identified and selected for the present work.

Trade-offs between accuracy and sensitivity of $\Delta\Phi$ measurement (small λ), desire for small beam cross-section (small λ), and affordability of the MWI apparatus (large λ), often occur in practice. For the chosen $f_{\mu w}$ range, λ_0 ranges from 3.41 - 3.66 mm, and since $a \sim 180$ mm $\gg \lambda_0$, the plasma boundary appears flat to the beam. The aperture (window) diameter $d_w = 26.6$ mm, so $\lambda_0/d_w \leq 0.14$ and the diffraction effects are expected to be tolerable. The reliability of this MWI technique is evident from the stability of $N_{e,MWI}$ vs swept $f_{\mu w}$ in figure 11. Deviations from the least squares fit line (red) indicate that the expected errors are very small in this case.

Quantitatively, $\langle N_e \rangle$ is determined as follows. For a single-pass beam (figure 4) that traverses the central chord \mathcal{S} connecting the entrance (S_{in}) and exit (S_{out}) windows of the chamber through the axis ($R = 0$) at fixed axial distance $z \cong 22$ cm from the top of the source module, $\Delta\Phi$ is the integral of the cumulative phase delay of the beam along the locus of infinitesimal intervals ds that constitute \mathcal{S} :

$$\Delta\Phi = \int_{S_{in}}^{S_{out}} (k_o - k_p) ds, \text{ where } k_o \equiv 2\pi/\lambda_o \equiv 2\pi f_{\mu w}/c, \quad (2.2)$$

$$\text{and } k_p(s) = k_o \left(1 - f_{pe}^2 / f_{\mu w}^2\right)^{1/2} = k_o \left(1 - N_e/N_c\right)^{1/2}. \quad (2.3)$$

Here, N_c is the critical "cut-off" density above which $f_{pe} > f_{\mu w}$, k_p becomes imaginary, and the beam no longer propagates. Note that k_p is, in general, a function of s through its dependence upon $N_e(s)$. Without loss of generality, we then write:

$$\Delta\Phi = k_o \int_{S_{in}}^{S_{out}} \left[1 - \left(1 - N_e(s)/N_c\right)^{1/2}\right] ds, \quad (2.4)$$

which is real if $N_e(s) \leq N_c$ for all s .

In practice, neither the maximum density $N_{e,max}$ nor the shape of the profile $N_e(s)$ is known *a priori*, but in an unmagnetized ICP at $P_{rf} \leq 1$ kW for $P_0 \leq 10$ mTorr it is safe to assume that $N_{e,max} \ll 10^{14} \text{ cm}^{-3} \cong N_c$, the cut-off density for an 88 GHz beam. At this frequency, $\lambda_0 = 0.35$ cm and $S = 2a = 35.5$ cm, so that $S/\lambda_0 \sim 10$ fringes. Thus, a change in k_p by 1% yields $\Delta\Phi \sim 36$ degrees, which is measurable to within $\pm 1\%$ with the network analyzer. Ease of evaluation of $\Delta\Phi$ occurs when $N_e \ll N_c$; the integrand of equation (2.4) is expanded in a Taylor series, and only the 1st order term is retained:

$$1 - \left(1 - N_e(s)/N_c\right)^{1/2} \cong 1 - \left[1 - N_e(s)/2N_c\right] = N_e(s)/2N_c \rightarrow \Delta\Phi \cong \left(k_o/2N_c\right) \int_{S_{in}}^{S_{out}} N_e(s) ds. \quad (2.5)$$

Note that $\Delta\Phi \cong \langle N_e \rangle / 2N_c \Rightarrow \langle N_e \rangle \cong 2N_c \Delta\Phi$, and thus the chord-averaged density is proportional to the phase shift in this approximation. In the happy circumstance that

$F_{norm}(0)$ is known (at least approximately) or perhaps even unity (better still), then the central density $N_e(0)$ is readily obtainable from $\Delta\Phi$. In general, $F_{norm}(0)$ must be determined through alternate means or via Abel inversion of a matrix of many chord-averaged MWI measurements, including off-axis chords that are prone to refraction and multiple beam path effects. This latter technique is expensive and usually impractical, particularly if chamber-width rectangular windows or alternate means of sampling an entire plasma cross-section are unavailable.

A compromise solution to the profile correction problem was adopted, whereby the usual Abel inversion procedure was used to calculate $N_e(0)$ using the *relative*, as opposed to *absolute*, values of $N_i(R)$ and $N_i(0)$ obtained with a radially scannable Langmuir probe in order to compute $F_{norm}(0)|_{LP} \equiv \{N_i(0)/\langle N_i \rangle\}|_{LP}$ using equation (2.1). *Provided that the actual normalization factor $F_{norm}(0)|_{actual} = F_{norm}(0)|_{LP}$, and (from above) $\langle N_e \rangle_{,MWI} = \langle N_e \rangle|_{actual}$, we may then relate the actual local electron density $N_e(0)|_{actual}$ to the measured $\langle N_e \rangle_{,MWI}$ as follows:*

$$N_e(0)|_{actual} = \frac{\langle N_e \rangle_{,MWI} \cdot N_i(0)|_{LP}}{\langle N_i \rangle|_{LP}} \equiv F_{norm}(0)|_{LP} \cdot \langle N_e \rangle_{,MWI}. \quad (2.6)$$

The success of this technique depends upon the ability of the probe to yield accurate *relative* measurements of $N_i(R)$ at all R along the chord. If the probe theory that is used to obtain $N_i(R)$ becomes invalid at some R or otherwise exhibits systematic error, then the measured $F_{norm}(0)|_{LP}$ may differ from $F_{norm}(0)|_{actual}$ and yield an inaccurate value of $N_e(0)|_{,MWI}$ from equation (2.6). An independent measurement of $N_p(0)$ $\{N_p(0)|_{other}\}$ is thus desired to ensure that gross errors are not thereby introduced. To this end, the POP method is employed in the present work. As will be discussed in Section (2.3), the POP itself may suffer from systematic error [26], but a lower bound of the accuracy of the Abel inversion technique can still be obtained for verification purposes.

It will be demonstrated *a posteriori* that the density profiles obtained as per above are very uniform over the majority of the plasma cross-section, and thus $\langle N_e \rangle \cong N_e(0)$ is readily determined. Using this local value of $N_e(0)$, a comparison is made with that obtained from the local POP method with the probe positioned at $R = 0$ along the chord subtended by the MWI beam path. *If satisfactory agreement is obtained between the MWI value $N_e(0)|_{,MWI}$ and the POP result $N_e(0)|_{,POP}$, then $N_e(0)|_{,MWI}$ is treated as the true $N_p(0)$ value to which all else will be compared.* Radial $N_i(R)$ profiles were obtained at each P_0 and P_{rf} using the scannable Langmuir probe, and the resulting curves were integrated to yield $F_{norm}(0)$ in each case. It was thus found that $\langle N_e \rangle \cong N_e(0)$ to within experimental error in all cases, probably due to the excellent uniformity of the ICP discharge. Figure 12 shows the results for the 5 mTorr case. Profile effects are henceforth ignored, but the POP technique is described in the next section.

2.3. Plasma Oscillation Probe (POP)

The Plasma Oscillation Probe (POP) method is, in principle, a robust way to make local measurements of N_e in a wide variety of operating regimes. Introduced by Sugai and co-workers [27] and demonstrated in the harsh RF and chemical environments of exotic processing plasmas such as electronegative gases [26], this method has been used for $N_p \sim 10^9 - 10^{11} \text{ cm}^{-3}$ in the low-medium pressure range of capacitive and inductively coupled RF-

plasmas. As shown in figure 13, the POP consists of a filament (e.g. tungsten) and an antenna (thin wire ~ 1 cm long), parallel to each other and in close (~ 1 cm) proximity. Enough filament current I_{fil} is supplied to make it glow (dull-to-bright red) and emit electrons, while sufficient negative filament bias voltage V_{fb} is applied with respect to the chamber so that the electrons stream towards the walls. If I_{fil} and V_{fb} are sufficiently large [26,27], an electron beam forms of sufficient energy $U_b = V_s - V_{fb}$ and density N_b to excite the classic two-stream instability [23]. Under those conditions where thermal effects can be neglected ($U_b/T_e > 20$, true in all cases herein), the frequency of the most unstable mode f_{osc} is given by the "weak beam" formula [28]:

$$f_{osc} \cong f_{pe} \left[1 - (\eta_b/16)^{1/3} \right] \cong f_{pe} \text{ if } \eta_b \equiv N_b/N_e \ll 1 \quad (2.7)$$

If this inequality is satisfied, f_{osc} is independent of N_b and U_b as long as the latter is also kept sufficiently small. Electron plasma oscillations are detected by the antenna, which is connected to an HP8592A spectrum analyzer. With proper care [26] a single narrow peak is observed (figure 14) at frequency $f_{osc} \cong f_{pe}$, related to N_e in convenient units as:

$$N_e (10^{10} \text{ cm}^{-3}) = 1.24 f_{pe} (\text{GHz})^2 \quad (2.8)$$

This simple formula is known to break down (a) at sufficiently high electron collision frequency f_{coll} such that $f_{coll}/f_{rf} \geq 0.1$ [26], and (b) when U_b (i.e. V_{fb}) is large enough to excite other modes besides the most unstable one. Also, if P_{rf} (and thus N_e) is too low, then the electron beam becomes a significant source of ionization and it undergoes self-oscillation within the tenuous plasma it creates (figure 15). In this filament-produced plasma ($P_{rf} = 0$), $f_{osc} = 783$ kHz (as indicated by the marker) yields $N_b = 7.6 \times 10^9 \text{ cm}^{-3}$.

In practice, the failure modes described above are readily detected as follows: modest changes in V_{fb} and slight changes in I_{fil} do not alter f_{osc} . If the peak moves sideways on the spectrum analyzer (f_{osc} shifts) as these parameters are varied, then it does not correspond to the desired mode, and the beam parameters must be readjusted until the candidate peak remains stationary. POP is robust in that f_{osc} is not altered by phenomena that typically interfere with other diagnostic techniques, most notably RF-induced V_s fluctuations that distort the characteristic curves from Langmuir probes that are not properly RF compensated [9]. However, if the oscillation is not already driven into saturation, such fluctuations may amplitude-modulate this electron plasma "carrier" frequency (by modulating U_b) and create sidebands at $f_{pe} \pm f_{rf}$, such as are commonly observed (figure 16). Furthermore, if N_p itself is RF-modulated, then split peaks may result (at say, f_1 & f_2) such that, in the specific example of figure 17,

$$\Delta N_e / N_e \cong (f_2^2 - f_1^2) / (f_{avg})^2 = (5.4/45.6)^2 \approx 1.5\% \quad (2.9)$$

If $N_e(t)$ modulation indeed occurred in this case, then the peak near 100 MHz could be the interference product of a pair of unstable modes, corresponding to $N_e(t_n)$ at times $t_n = t_0$ and $t_0 + 1/(2f_{rf})$ at which $V_s(t_n)$ reaches its maximum and minimum values (respectively) within one RF cycle. In many cases [e.g. $V_s(t) \propto \sin(2\pi f_{rf} t)$], the plasma parameters are quasi-stationary at times t_n corresponding to such extrema, so that the plasma appears to os-

cillate between the two quasi-stable states. Such an effect could, in principle, be detected by mixing the MWI mixed/detected phase signal $\Delta\Phi(t)$ with an RF reference signal, but this is beyond the scope of the present work. Alternatively, modulation of $N_e(t)$ at frequency $f \neq f_{rf}$ could yield similar features in the POP spectrum, provided that $N_e(t)$ is quasi-stationary at specific times τ corresponding to adjacent $N_e(t)$ extrema. Note that this $N_e(t)$ modulation hypothesis hinges upon the persistence of the beam-plasma instability over a time interval $\Delta\tau \geq 1/(2f)$; otherwise no interference would be observed between the two modes.

In contrast to figure 17, the case depicted in figure 18 is that of a purposefully overdriven mode; $V_{fil} = 230V$ and U_b are more than double the values required to generate a single peak. A split peak at $f_{osc} = f_0 \pm \delta f$ is observed, with central frequency $f_0 \cong 2.6$ GHz and frequency difference $\delta f \cong 30$ MHz. These features are relatively broad and indistinct, in contrast to the well-defined narrow peaks of figure 17. Furthermore, a broadband "skirt" is observed around $f_{osc} = 0$ in figure 18, whereas a narrow low frequency peak that appears to be an interference product of the two distinct peaks at $f_{osc} \sim 1.9$ GHz appears in figure 17. This finding suggests that multiple peaks are not automatically attributable to overdriving of the beam, and are consistent with the hypothesis of a peak splitting mechanism due to temporal modulation of N_p , as per the preceding discussion.

In the present work, POP is used merely to confirm the validity of the Abel inversion method used to extract $N_e(0)$ from $\langle N_e \rangle_{MWI}$ measurements. It can then be determined by comparison which probe theory is the most accurate. Although it is apparent from the above discussion that the POP method is not perfectly understood, it is nevertheless sufficient for the task at hand.

3. Floating Potential Method

As previously discussed (figure 10), it is found that the three main classical collisionless probe theories (ABR, BRL and OML) yield different results for $N_i(0)$, none of which exhibit good agreement with the reliable $N_{e,MWI}$ results for all operating regimes in the present study. Previews of the comparison with OML are shown in figure 19a. It is observed that OML consistently overestimates N_i , and the ordering $N_{e,Ies} \leq (N_{e,MWI}, N_{e,POP}) \leq N_{i,OML}$ recurs; these observations are consistent with previously reported results [10,11,18,24,26,27,29]. This divergence of N_i results is possibly due to the fact that collisions actually do occur in real plasmas that can destroy the ion angular momentum that OML and BRL assume to be conserved. Such an effect would increase the ion current [30] over that predicted by OML or BRL theory, resulting in an overestimation of $N_{i,OML}$ and $N_{i,BRL}$ over their true values. Collisions could also cause ions to deviate from their (presumed) collisionless trajectories within the presheath, thereby reducing their flux to the probe tip--an effect which is not accounted for in the ABR or BRL theories.

It will be shown, however, that the best agreement with experiment is obtained from none of the classical probe theories mentioned above. Instead, we adopt an alternative heuristic approach; it is *postulated* that I_i in the ion saturation region ($V_0 \gg T_e$) is largely determined by the expansion of the Child-Langmuir (CL) ion sheath [22] surrounding the tip. It is further *assumed* that this sheath constitutes an absorption region of area A_{sh} ; it then follows that $I_i \propto A_{sh} = \text{effective tip area}$. It remains to show how A_{sh} varies with V_0 in order to determine the dependence of I_i upon V_0 . In its simplest one-dimensional form, the Child-

Langmuir formula for the ion sheath thickness $X_{sh} \propto V_0^{3/4}$; it will be seen that, to a good approximation, $I_i \propto V_0^{3/4}$ in the ion saturation regime; a preview of the comparison of all of the N_i results, including $N_{i,CL-Vf}$ thus obtained, is shown in figure 19b. In general, the ordering $N_{i,ABR} \leq (N_{e,MWL}, N_{i,CL-Vf}, N_{i,OML}) \leq N_{i,BRL}$ is observed throughout.

The 1-D formula for the CL sheath thickness X_{sh} as a function of the normalized probe bias voltage $\eta \equiv -(V_b - V_s)/kT_e$ is given by [23,24,31]:

$$X_{sh} = \frac{\sqrt{2}}{3\alpha_0} (2\eta)^{3/4} \lambda_D \cong 1.02\eta^{3/4} \lambda_D \cong \eta^{3/4} \lambda_D. \quad (3.1)$$

Other authors have derived similar formulas, differing mostly in the way the boundary conditions at the sheath edge are treated [31,32], but use of these more sophisticated expressions does not improve the results. Further assuming that the absorption region is a cylindrical shell consisting of a probe tip of radius R_p surrounded by a CL sheath with thickness X_{sh} given by equation (3.1), we write:

$$A_{sh} \cong 2\pi(X_{sh} + R_p)L_p = A_p(1 + X_{sh}/R_p) \cong 2\pi L_p X_{sh}, \quad \text{for } R_p \ll X_{sh} \ll L_p. \quad (3.2)$$

Substitution of X_{sh} from equation (3.1) into (3.2) yields:

$$A_{sh} = 2\pi L_p (R_p + \eta^{3/4} \lambda_D) \quad . \quad (3.3)$$

$$I_i(\eta_f) = 2\pi (R_p + \eta_f^{3/4} \lambda_D) L_p \alpha_0 N_i u_B. \quad (3.4)$$

Substitution of $\lambda_D \equiv [\epsilon_0 T_e / e N_e]^{1/2}$ into (3.4) yields an analytical expression for N_i :

$$N_i = \left\{ \left(-B + B \left[1 + (C/B^2) \right]^{1/2} \right)^2 \right\}, \quad \text{where } B \equiv \frac{\eta_f^{3/4}}{R_p} \left(\frac{\epsilon_0 T_e}{e} \right)^{1/2} \text{ \& } C \equiv \frac{I_i(\eta_f)}{2\pi R_p L_p \alpha_0 u_B} \quad (3.5)$$

Note that N_i may now be solved for in terms of T_e , V_f , V_s and $I_{ion-fit}(V_f) \equiv I_i(V_f)$, provided that the latter quantity can be ascertained from the I - V curve. Strictly speaking, V_s by itself need not be known, since it only appears in equation (3.5) through the expression for η_f , the normalized floating potential. In any case, V_f is immediately obtained from the I - V curve, and values for T_e and V_s can in principle be found from the natural logarithm of $I_e = I_p - I_{ion-fit}$ (below) and from dI_p/dV_b in a straightforward fashion. Since the validity of the CL law for the sheath thickness has been assumed as an initial ansatz, inspection of equation (3.4) in the thick sheath limit ($R_p \ll \eta_f^{3/4} \lambda_D$) yields $I_i^{4/3} \propto V_0$, indicating that a linear regression fit ($I_{ion-fit}$) of $I_i^{4/3} \propto V_0$ is in order. Extrapolation of said fit to $V_b = V_f$ yields a value of $I_{ion-fit}(V_f) \equiv I_i(V_f)$ from which N_i can be determined. Note that this technique is novel in that it relies on the accuracy with which the ion current at V_f can be *inferred* through extrapolation rather than on a directly measurable quantity. The success of this "floating potential method" [22,32] is probably due to the fact that the extrapolation need be valid only for a relatively small excursion from the region of the I - V curve for which $I_i \gg I_e$, as opposed to other methods that require precise knowledge of V_s or are more sensitive to the estimate of T_e that is used in the calculations.

Figure 20 illustrates the use of this Child-Langmuir floating potential (CL- V_f) method in the analysis of I_i from a Langmuir probe. In this example ($P_0 = 5$ mTorr and $P_{rf} = 900$ W), the functional dependence of $I_p(V_0)$ according to (a) OML and (b) CL- V_f is evaluated by plotting the single power laws I_p^x vs V_0 for $x = 2$ and $x = 4/3$, respectively, then comparing the quality of the fits. Note the remarkable improvement in (b) over (a), suggesting that the CL- V_f method is the more applicable of the two in this case. It must be noted that an additional constraint is imposed in the OML case, namely that $I_i \rightarrow 0$ as $V_b \rightarrow V_s \cong 14.2$ V as measured previously using the Druyvestyn approach; this constraint *must* be imposed since it follows directly from the OML formula {equation (1.2)}. No constraint is imposed in the CL- V_f case; the CL sheath must collapse for $V_b > V_s - T_e / 2$ because the Bohm sheath criterion cannot be satisfied.

An excellent fit of the $I_i^{4/3}$ power law to the data is shown in figure 20b. More details concerning the rationale for this approach are presented in a companion paper [32]. Inversion of the $I_p^{4/3}$ curve of figure 20b back to $I_p \cong I_{ion-fit}$ vs V_b yields figure 20c, whereby a value of $I_i(V_b) \cong I_{ion-fit}(V_b)$ is obtained by inspection of the graph. Subtraction of this $I_{ion-fit}(V_b)$ fit from I_p yields an approximation to I_e , the electron component of the total current. Taking the natural logarithm of I_e yields figure 20d, which appears to be linear (nearly exponential behavior) over a much larger interval in V_b (-7 V $< V_b < 10$ V) than in the corresponding I_i^2 power law case of figure 9. In this case, apparently the $I^{4/3}$ power law fit more accurately models the ion contribution to the total probe current. A least squares fit to said interval is obtained (red line of figure 20d), the slope of which ($= 1/T_e$) yields $T_e \cong 2.84$ eV. Substitution of T_e into equation (3.5), together with $I_i(V_b)$ from above, yields a value for N_i ($\equiv N_{i,CL-V_f}$), which is then compared with the corresponding quantities ($N_{i,ABR}$, $N_{i,BRL}$ and $N_{i,OML}$) obtained using the classical probe theories described above. Such a procedure is used to generate the $N_{i,CL-V_f}$ points of figure 19b and figure 21, which exhibit the best overall agreement with experiment of all of the methods of determination of N_i from I_p considered herein.

4. Results and Discussion

Figure 21 summarizes the results of the density measurements for the entire 20-element experimental matrix of operating parameters sampled in the current study. Density measurements from all of the diagnostics are included here. For ease of comparison, the probe results obtained from the BRL and ABR analyses are excluded from these graphs; we merely note that BRL (ABR) continually overestimates (underestimates) N_p by $\sim 2x$, as in the case of figures 10 and 19b. ESPsoft™ is used to extract I_i from the $I-V$ curves to yield $N_{i,OML}$. Excellent agreement is observed between $N_{e,POP}$ and the true $N_{e,MWI}$ values for $P_0 \leq 2$ mTorr. However, for $P_0 \geq 5$ mTorr, $N_{e,POP}$ consistently falls on or below $N_{e,MWI}$, and lies above the $N_{e,Ies}$ results. As shown in the figures, the CL- V_f approach yields the best agreement between the Langmuir probe results and MWI throughout the range of parameters covered in the present work. Indeed, $N_{i,CL-V_f}$ falls within the error bars of $N_{e,MWI}$ in all cases. It is not known for certain at present how such a remarkable degree of accuracy is obtained from this non-rigorous approach, but these figures provide overwhelming evidence that the extrapolation of the $I_i^{4/3}$ fit to $V_b = V_f$ is indeed the correct approach. Further discussion may be found in the companion theoretical work [32]. Many results obtained over the years are

also confirmed here: $N_{i,OML}$ consistently overestimates N_p for all but the highest P_0 and P_{rf} . Indications are that $N_{i,OML}$ exhibits good agreement with $N_{e,MWI}$ by accident [10] for $P_0 \approx 10$ mTorr. $N_{i,ABR}$ results are the lowest of all.

Apparently, the POP technique is more accurate than the Langmuir probe method when OML theory ($N_{i,OML}$) or the electron saturation current (I_{esat}) method ($N_{e,Ies}$) is applied in the low- P_0 cases. It has been noted [26,27] that POP yields values of $N_e \sim 40\%$ higher than N_e from Langmuir probes, and $\sim 30\text{-}50\%$ lower than N_i from Langmuir probes when BRL is used. This discrepancy was attributed to probe aberrations such as electron reflection and reemission from the tip, secondary electron emission, etc. In the present study, it is also observed that $N_{e,Ies} \leq N_{e,POP} \leq N_{i,OML}$, in apparent agreement with previous authors, which would seem to corroborate the previous findings. However, note that $N_{e,POP} \leq N_{e,MWI}$ throughout the parameter range of the present work as well. Treating the MWI results $N_{e,MWI}$ as true, reliable values of N_p , we therefore conclude that POP suffers from a systematic error, in that it yields results that are consistently lower than the true values, the degree of deviation increasing with P_0 and/or N_p as well. Since the causes of probe-related aberrations mentioned above cannot affect the MWI measurements, we deduce that another mechanism is responsible for the discrepancy between the POP results and the Langmuir probe values at higher P_0 and/or N_p . In order to narrow down the cause still further, we note that the discrepancy between the $N_{e,POP}$ and $N_{e,MWI} / N_{i,OML}$ results is much larger at $P_0 = 10\text{mTorr}$ than at 5mTorr , even when cross-comparisons between the two data sets for points with approximately equal N_p are made. This finding strongly indicates that it is P_0 , and not N_p , which is associated with the apparent systematic error in the POP method. Despite this complication, POP proved to be very useful for the purposes of the present work.

5. Summary and Conclusions

A definitive experimental evaluation of ion density measurement techniques based on Langmuir probes is performed in an RF-produced ICP reactor, in which the classical theories of ion collection current I_i to a Langmuir probe are tested over a wide range of plasma parameters. In particular, ABR, BRL and OML theories are evaluated as to their predictive power in the determination of N_i over the wide range of parameter space thus obtained. Accurate values of central electron density $N_e(0)$ are obtained in Ar from chord-averaged $\langle N_e \rangle$ measurements using MWI and Abel inversion of the radial profile $N(R)$ obtained from Langmuir probes. Density profiles were highly uniform, so that a correction to the chord-averaged MWI results for $\langle N_e \rangle$ was unnecessary. Results are compared to those obtained from the PO) method. Reliable values of $N_{e,MWI}(0)$ thus obtained are compared with $N_i(0)$ from theoretical analyses of the I-V curves obtained with a Langmuir probe, as well as with $N_{e,Ies}(0)$ from electron saturation current $I_e(V_s)$.

ABR theory consistently yields $N_i(0)$ values that are too low, and BRL overestimates $N_i(0)$ as well. OML exhibits the highest degree of agreement with experiment of all three classical ion collection current theories, but the accuracy of the OML values is observed to decrease markedly with decreasing P_0 . This observed trend is inconsistent with the physical picture of OML, since it is presumably collisions that make I_i deviate from its expected values, which should lead to better agreement as P_0 decreases. Therefore, the inapplicability of OML theory is reaffirmed, whereas it is conceded that I_i vs $V_0^{1/2}$ yields a reasonable fit in

some cases, albeit by accident. However, the best results are obtained by using a heuristic floating potential method, whereby $I_i^{4/3} \propto V_b$ is observed and attributed to the expansion of the Child-Langmuir sheath as V_b is driven into the ion saturation region. This simple technique for determining $N_i(0)$ from an extrapolation of an $I_i^{4/3}$ vs V_b linear regression fit to the value $I_{ion-fit}(V_f) \equiv I_i(V_f)$ evaluated at the floating potential V_f , and subsequent solution of a resulting quadratic equation, is demonstrated. Excellent agreement between this CL- V_f method and the MWI and POP results are observed in most cases, and CL- V_f still outperforms the classical probe theories in the remaining instances. Further studies are necessary to determine the limits of applicability of this approach.

Acknowledgments

The authors wish to thank Hiden Analytical, Inc., for the use of their probe and their employee in this work, and also Brendan Melia of Hiden, and F. Matt Espiau of the UCLA Center for High Frequency Electronics for their valued technical support. We also thank Dave Johnson and John Donohue of PlasmaTherm[®] (now Unaxis[®]) for the use of the ICP source module.

References

- 1) Improved version available--ESPion[®] electrostatic probe, Hiden Analytical Ltd., Warrington, England: <http://www.hiden.co.uk/plasma.html>
- 2) Langmuir I 1923 *J. Frank. Inst.* **196** 751.
- 3) Allen J E, Boyd R L F, and Reynolds P 1957 *Proc. Phys. Soc. London* **B 70**, 297.
- 4) Bernstein I B and Rabinowitz I N 1959 *Phys. Fluids* **2** 112.
- 5) Chen F F, Etievant C, and Mosher D 1968 *Phys. Fluids* **11**, 811.
- 6) Lam S H 1965 *Phys. Fluids* **8** 73.
- 7) Laframboise J G 1966 *Institute for Aerospace Studies, Univ. of Toronto UTIAS Rep. No. 100*.
- 8) Mott-Smith H M and Langmuir I 1926 *Phys. Rev.* **28** 727.
- 9) Godyak V A 1990 in *Plasma-Surface Interactions and Processing of Materials* ed O Aucellio et al (Boston, Kuwer Academic).
- 10) Chen F F 1965 *J. Appl. Phys.* **36** 675.
- 11) Tuszewski M and Tobin J A 1996 *Plasma Sources Sci. Tech.* **5** 640.
- 12) Chen F F 2001 *Phys. Plasmas* **8** 3029.
- 13) Druyvesteyn M J 1930 *Z. Phys.* **64** 781.

- 14) Hershkowitz N 1989 in *Plasma Diagnostics Vol. 1*, ed O. Auciello and D.L. Flamm (New York: Academic Press).
- 15) Godyak VA, Piejak R B, and Alexandrovich B M 1993 *J. Appl. Phys.* **73** 3657.
- 16) Loewenhardt P, Zawalski W, Ye Y, Zhao A, Webb T R, Tajima D, and Ma D X 1999 *Jap. J. Appl. Phys.* **38** 4362.
- 17) Lho T, Hershkowitz N, Kim G H, Steer W, and Miller J 2000 *Plasma Sources Sci. Tech.* **9** 5.
- 18) Sudit I D and Woods RC, *Rev. Sci. Instrum.* **64** 2440.
- 19) Limpaecher L and MacKenzie K R 1973 *Rev. Sci. Instrum.* **44** 426.
- 20) Lamm A J, Leung K N, and Samec T K 1975 *Phys. Lett.* **51A** 490.
- 21) Chen F F and Evans J D 2000 *Proceedings of the International Congress on Plasma Physics (Quebec City, Canada)* p 908.
- 22) Evans J D, Zawalski W, and Chen, F F 2000 *Bull. Am. Phys. Soc.* **45** 146.
- 23) Chen F F 1984 *Introduction to Plasma Physics and Controlled Fusion* (New York: Plenum Press).
- 24) Lieberman M A and Lichtenberg A J 1994 *Principles of Plasma Discharges and Materials Processing* (New York: Wiley) p 173.
- 25) Wharton C B 1965, in *Plasma Diagnostic Techniques*, Huddleston R H and Leonard S L, eds. (New York: Academic Press).
- 26) Schwabedissen A, Benck E C, and Roberts J R 1998 *Plasma Sources Sci. Tech.* **7** 119; Schwabedissen A et al 1999 *Plasma Sources Sci. Tech.* **8** 440.
- 27) Shirakawa T and Sugai H 1993 *Jap. J. Appl. Phys.* **32**, 5129; Ahn T H, Nakamura K, and Sugai H 1995 *Jap. J. Appl. Phys.* **34** L1405.
- 28) Thompson J R 1971 *Phys. Fluids* **14** 1532.
- 29) Tonks L and Langmuir I 1929 *Phys. Rev.* **34** 876.
- 30) Trunec D 1998 *Proc. ICPP & 25th EPS Conf. On Contrl. Fusion and Plasma Physics* (Prague, Czech Republic: [publishers]) p 1506.
- 31) Hutchinson I H 1987 *Principles of Plasma Diagnostics* (Cambridge Univ. Press) p 61.
- 32) Chen F F, Evans J D, and Arnush D 2002 *Phys. Plasmas* at press.

Figure Captions

Figure 1: Orbital motion model. Ions with sufficient angular momenta follow open (free) trajectories; the rest are collected. An absorption region of radius $R_a \geq R$ surrounds the probe tip.

Figure 2: Orbital Motion Limited (OML) theory applies in the absence of an absorption radius.

Figure 3: PlasmaTherm[®] ICP source module on top of a magnetic bucket. A 3-turn spiral antenna is wrapped around a ~ 1 cm thick ceramic liner which contains the plasma it creates when energized with RF. Hiden[®] ESP[™] Langmuir probe (right) and the POP (left) are visible through a MWI access window – all diagnostics sample the region $R \cong 0$, at axial distance $z \cong 22$ cm from the top of the source. Machine parameters: module i.d.=32cm, module-bucket interface at $z = 16.4$ cm, bucket i.d. = 35.5cm, bucket height = 20.5 cm, RF power $P_{rf} = 300 - 900$ W, neutral pressure $P_0 = 1-10$ mT Ar, plasma density $N_p = 4 \times 10^{10} - 5 \times 10^{11}$ cm⁻³ and electron temperature $T_e = 2 - 4$ eV.

Figure 4: Conceptual cutaway (top) view of experimental setup, including the essential elements of the diagnostics. Also shown (dotted lines) is the plasma volume subtended by the MWI signal beam path \mathcal{S} , which encompasses the region sampled by the POP and Langmuir probes.

Figure 5: Schematic diagram of Hiden ESP[™] commercial Langmuir probe.

Figure 6: Typical Langmuir probe I-V characteristic. $P_0 = 5$ mTorr, $P_{rf} = 900$ W.

Figure 7: 1st derivative of the $I-V$ curve of Fig. 6. A single peak is observed at $V_b \cong 14.2$ V $\equiv V_s$, the plasma space potential, according to the Druyvestyn method.

Figure 8: I_p^2 vs V_b , as generated by squaring the curve from Figure 7. Linear regression over a user-defined interval yields a reasonable ion current fit $I_{ion-fit}$ (dashed line) except at large $-V_b$.

Figure 9: $\ln(I_e)$ vs V_b , with least squares fit line evaluated in the electron retardation region (red dashed); interval is chosen manually by the user. T_e is the reciprocal of the slope: ~ 2.7 eV in this case.

Figure 10. N_p vs P_{rf} , for $P_0 = 5$ mTorr; N_i using BRL, OML and ABR-based algorithms on $I-V$ curves. OML yields the best agreement of the three classical probe theories with the true $N_{e,MWI}$ values.

Figure 11: Example of $\langle Ne \rangle_{MWI}$ versus $f_{\mu w}$ over the interval 82-88 GHz, indicating the stability of $\Delta\Phi$ with respect to swept $f_{\mu w}$. Good statistics achieved by sweeping $f_{\mu w}$.

Figure 12: Calibration of $N_e(0)$ from MWI using Abel inversion of $N_i(r)$ from the radially scannable Langmuir probe. "Corrected" $N_e(0)$ and "uncorrected" (Abel inversion not incorporated) $\langle Ne \rangle$ vs P_{rf} : $P_0 = 5$ mTorr. Both data sets fall within the error bars; similar results obtained for all P_0 .

Figure 13: Schematic of POP apparatus, consisting of a filament, an antenna, bias/filament supplies and spectrum analyzer. V_{fb} is applied between probe and chamber to accelerate the electron beam.

Figure 14: Typical POP signal on spectrum analyzer. Peak at $f_{osc} = 2.095$ GHz yields $N_e = 5.4 \times 10^{10} \text{ cm}^{-3}$. A narrow peak occurs if minimal V_{bf} and I_{fil} are supplied to excite the beam-plasma mode.

Figure 15: POP spectrum of tenuous, localized plasma produced by filament/e-beam only. $P_{rf} = 0$.

Fig. 16a: Single, but broad, POP peak at $f_{osc} = 2.023$ GHz. Note "skirt" near $f = 0$.

Fig. 16b: Same as (a), but f -scale expanded - sidebands at f_{rf} and harmonics observed.

Fig. 17: Two narrow POP peaks centered at ~ 2.1 GHz and ~ 100 MHz apart. Note presence of 100MHz signal and several harmonics as well, possibly due to N_p modulation by RF.

Figure 18: Broad POP split peak due to an overdriven electron beam. $V_{fb} = 230$ V, $I_{fil} = 6.8$ A, more than double the values that yield a single, narrow peak. Broadband skirt near $f = 0$, indicating broadband beating with f_{rf} . $P_0 = 1$ mTorr, $P_{rf} = 450$ W.

Figure 19a: Same as figure 10, but with $N_{e,POP}$ and $N_{e,Ies}$ from the Langmuir probe for comparison with $N_{e,MWI}$. $N_{e,Ies} \leq (N_{e,MWI}, N_{e,POP}) \leq N_{i,OML}$, as previously reported in the literature.

Figure 19b: Same conditions as (a), but just the N_i results from classical Langmuir probe theories and $N_{i,CL-Vf}$ from the Child-Langmuir floating potential approach. $N_{i,CL-Vf}$ yields excellent agreement with $N_{e,MWI}$. BRL represents an upper bound on the theoretical N_i , whereas ABR is the lower bound.

Figure 20a: I^2 vs V_0 fit (line) of the I - V curve (dots) obtained for $P_0 = 5$ mTorr, $P_{rf} = 900$ W. Adherence to OML imposes the constraint $I_i \rightarrow 0$ as $V_b \rightarrow V_s \cong 14.2$ V obtained from the 1st derivative.

Figure 20b: $I^{4/3}$ vs V_0 fit (red) of the same I - V curve (dots) as in (a). Note the high quality of the fit and that no constraint on I_i at the V_b -intercept is imposed.

Figure 20c: Inversion of the $I^{4/3} \propto V_0$ fit from (b), plotted as I_{ion_fit} (line) with the I_p data (dots). $I_i(V_f)$ is found by extrapolation of the fit to $V_b = V_f$, and then plugged into equation (3.5) to yield $N_{i,CL-Vf}$.

Figure 20d: $\text{Ln}(I_e)$ vs V_b , where $I_e = I_p - I_{ion_fit}$, as calculated from the CL- V_f method. A high quality linear fit is obtained over a fairly wide interval $-7 \text{ V} < V_b < 10$ V, yielding $T_e = 2.85$ eV.

Figure 21a: Comparison of N_p from (a) MWI - $N_{e,MWI}$, (b) POP - $N_{e,POP}$, and the Langmuir probe--the latter using (c) OML - $N_{i,OML}$, (d) the CL- V_f algorithm-- $N_{i,CL-Vf}$, and (e) electron saturation current-- $N_{e,Ies}$. The ordering $N_{e,Ies} < (N_{e,POP}, N_{e,MWI}, N_{i,CL-Vf}) < N_{i,OML}$ is observed. Here, $N_{i,POP} \cong N_{e,MWI}$ and $N_{e,MWI} \cong N_{i,CL-Vf} < N_{i,OML}$ at all P_{rf} .

Figure 21b: Same as Figure 21a, but for $P_0 = 2$ mTorr. Same results, except that the success of the CL- V_f approach is more apparent, as is the convergence of the MWI, POP and CL- V_f results.

Figure 21c: Same, but for $P_0 = 5$ mTorr. Note the systematic deviation of $N_{e,POP}$ from the $N_{e,MWI}$ result, and the convergence of the $N_{i,CL-Vf}$ and $N_{e,MWI}$ values, as P_{rf} increases.

Figure 21d: Same, but for $P_0 = 10$ mTorr. The ordering $N_{e,Ies} < N_{e,MWI}, N_{e,POP} < N_{i,OML}$ is violated for the first time, for $P_{rf} \geq 600$ W. Deviation of $N_{e,POP}$ from $N_{e,MWI}$ increased dramatically from the 5 mTorr case. $N_{i,CL-Vf}$ agrees with $N_{e,MWI}$ to within experimental error in all cases.

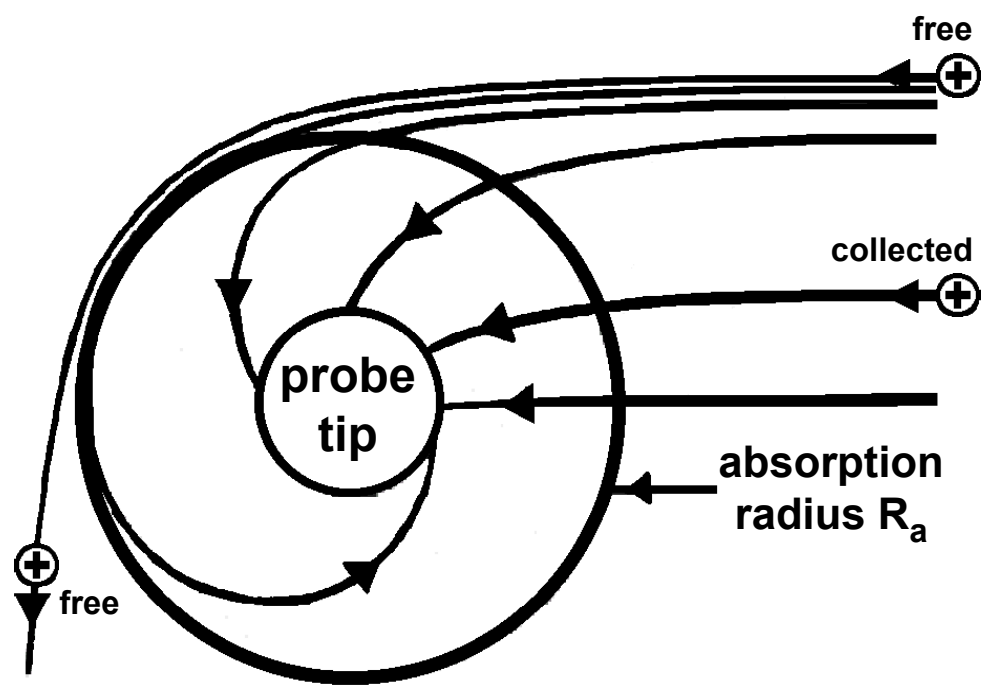


Figure 1: Orbital motion model. Ions with sufficient angular momenta follow open (free) trajectories; the rest are collected. An absorption region of radius $R_a \geq R$ surrounds the probe tip.

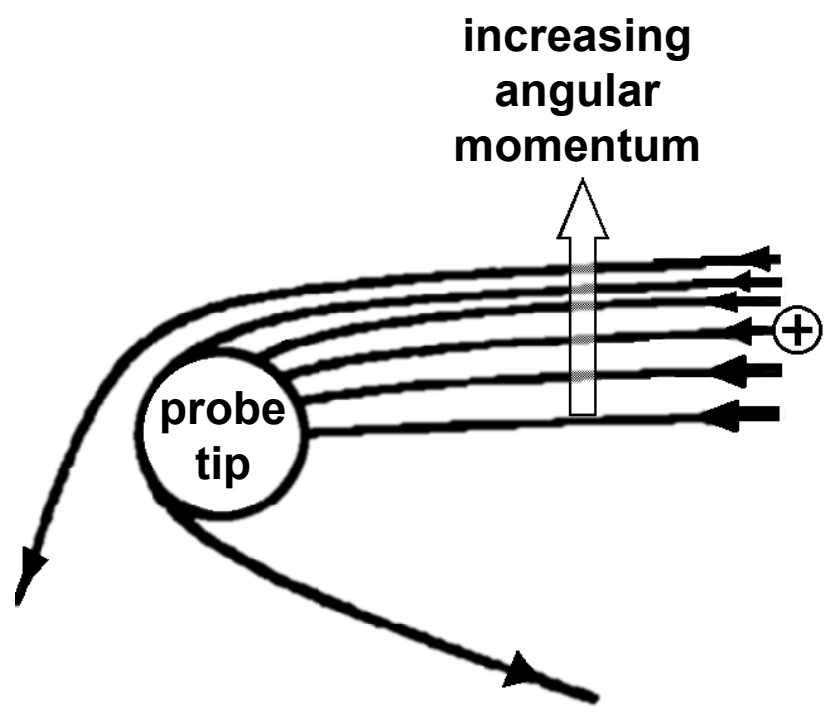


Figure 2: Orbital Motion Limited (OML) theory applies in the absence of an absorption radius.

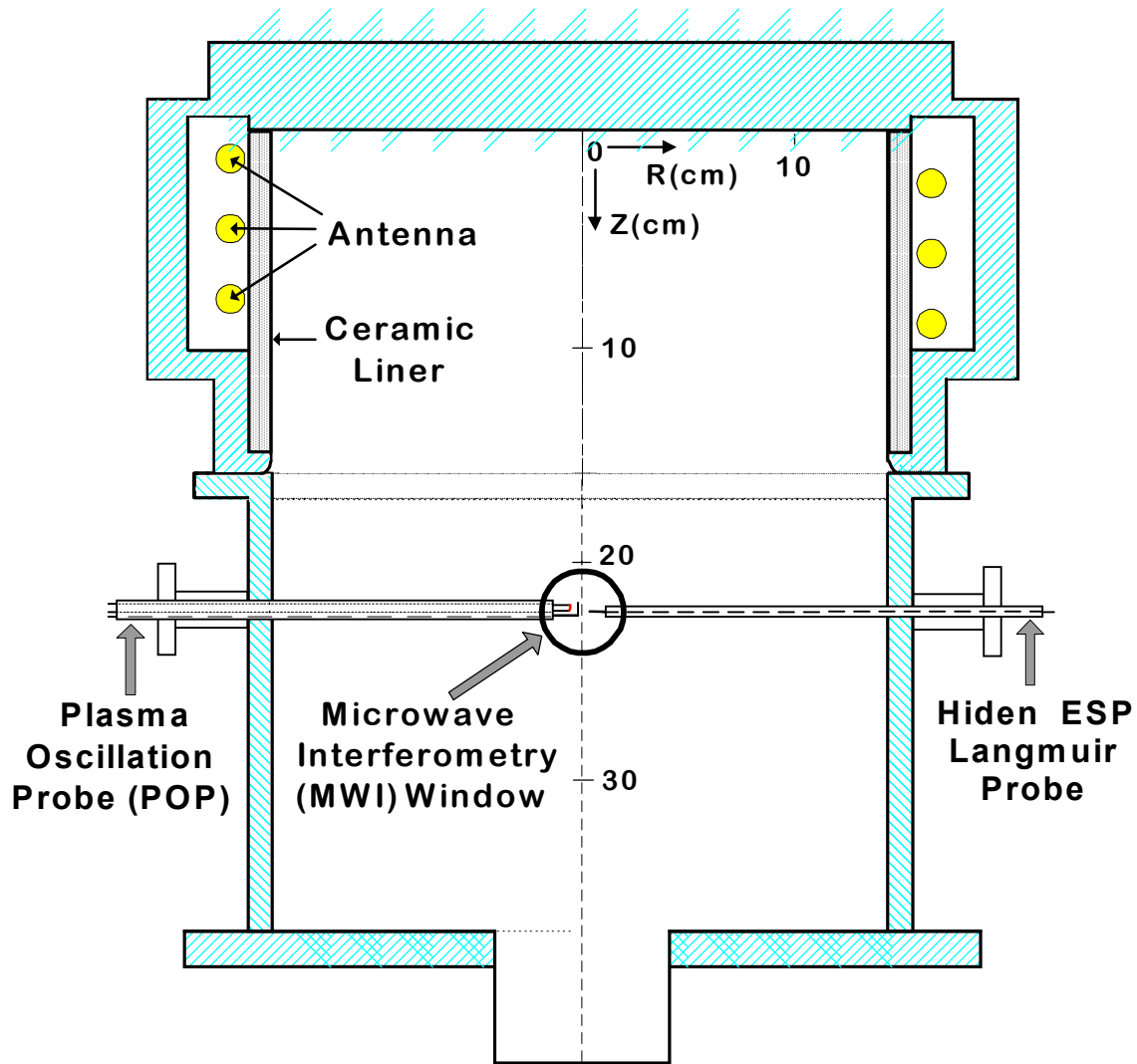


Figure 3: PlasmaTherm[®] ICP source module on top of a magnetic bucket. A 3-turn spiral antenna is wrapped around a ~ 1 cm thick ceramic liner which contains the plasma it creates when energized with RF. Hiden[®] ESP[™] Langmuir probe (right) and the POP (left) are visible through a MWI access window – all diagnostics sample the region $R \cong 0$, at axial distance $z \cong 22$ cm from the top of the source. Machine parameters: module i.d.=32cm, module-bucket interface at $z = 16.4$ cm, bucket i.d. = 35.5 cm, bucket height = 20.5 cm, RF power $P_{rf} = 300 - 900$ W, neutral pressure $P_0 = 1-10$ mT Ar, plasma density $N_p = 4 \times 10^{10} - 5 \times 10^{11} \text{ cm}^{-3}$ and electron temperature $T_e = 2 - 4$ eV.

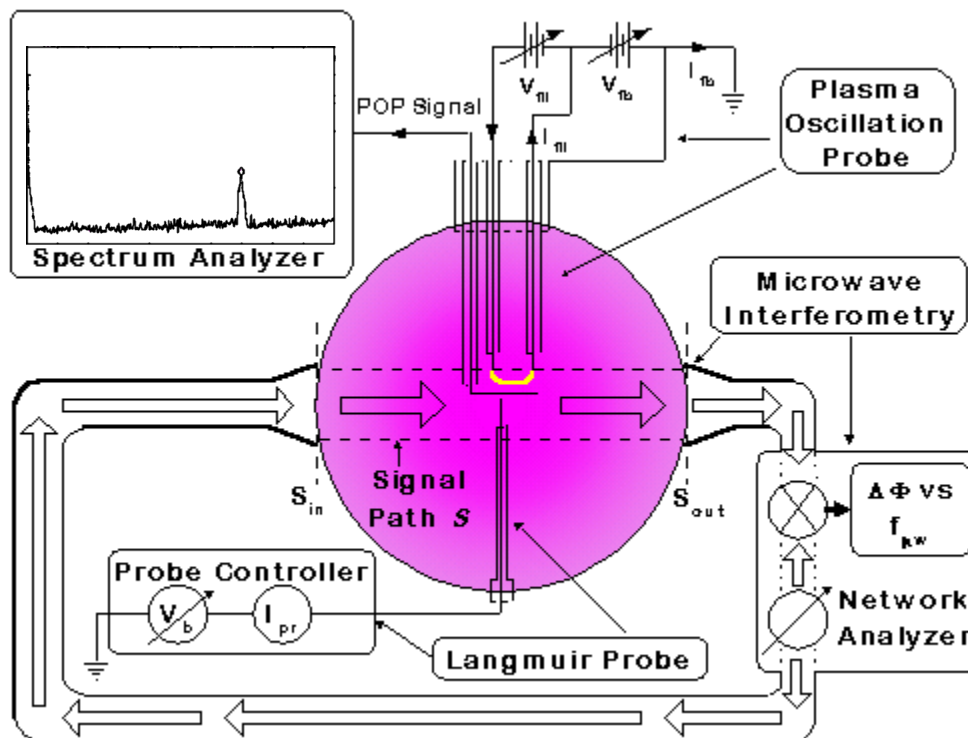


Figure 4: Conceptual cutaway (top) view of experimental setup, including the essential elements of the diagnostics. Also shown (dotted lines) is the plasma volume subtended by the MWI signal beam path S , which encompasses the region sampled by the POP and Langmuir probes.

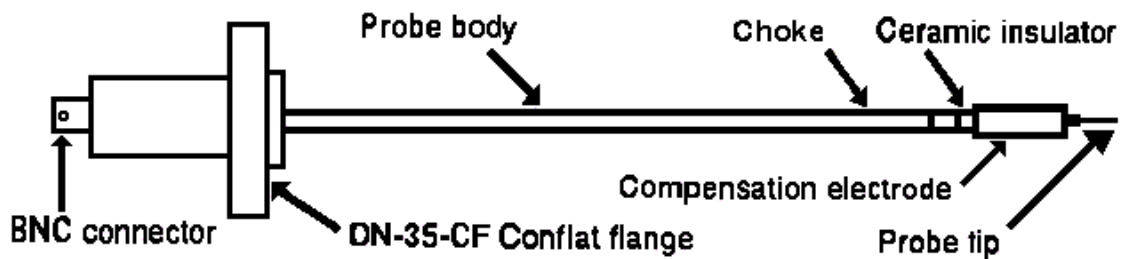


Figure 5: Schematic diagram of Hiden ESP™ commercial Langmuir probe.

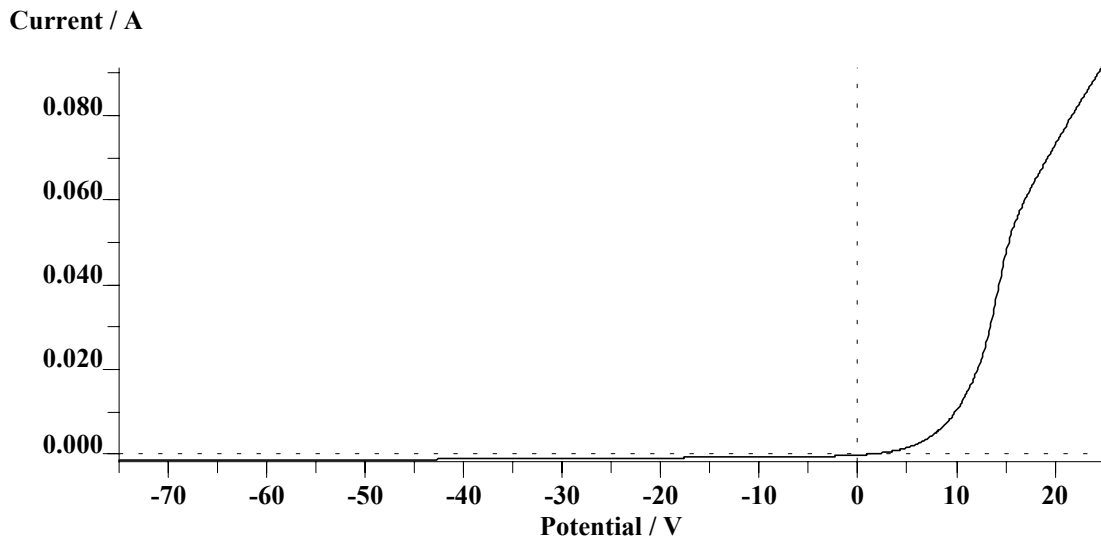


Figure 6: Typical Langmuir probe I-V characteristic. $P_0 = 5$ mTorr, $P_{rf} = 900$ W.

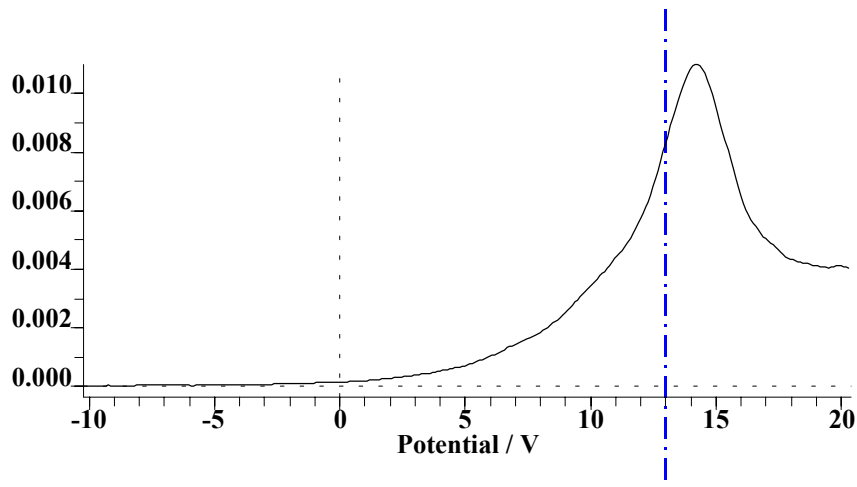


Figure 7: 1st derivative of the $I-V$ curve of Fig. 6. A single peak is observed at $V_b \cong 14.2$ V $\equiv V_s$, the plasma space potential, according to the Druyvestyn method.

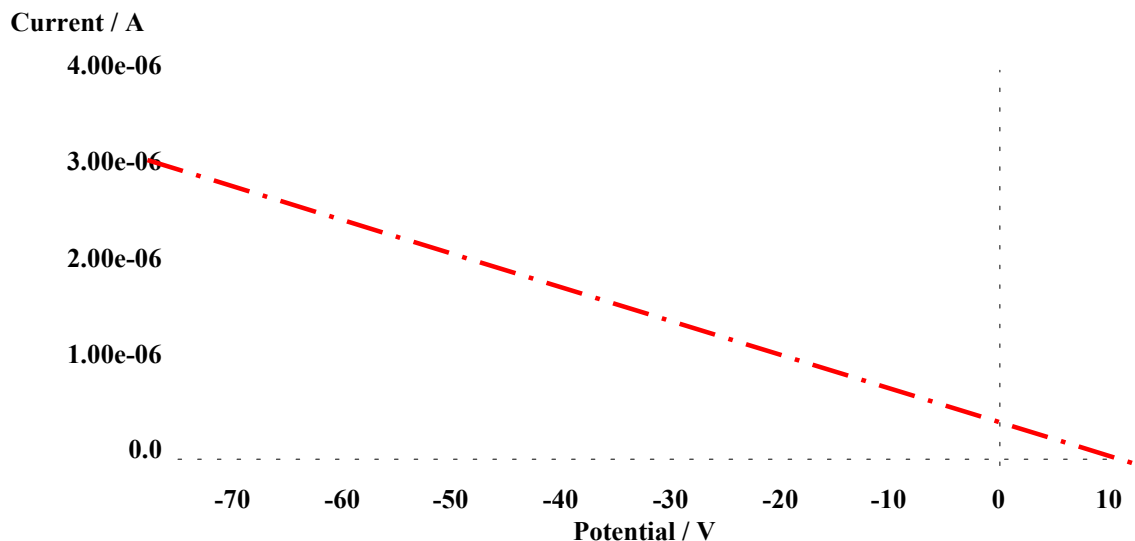


Figure 8: I_p^2 vs V_b , as generated by squaring the curve from Figure 7. Linear regression over a user-defined interval yields a reasonable ion current fit $I_{\text{ion-fit}}$ (dashed line) except at large - V_b .

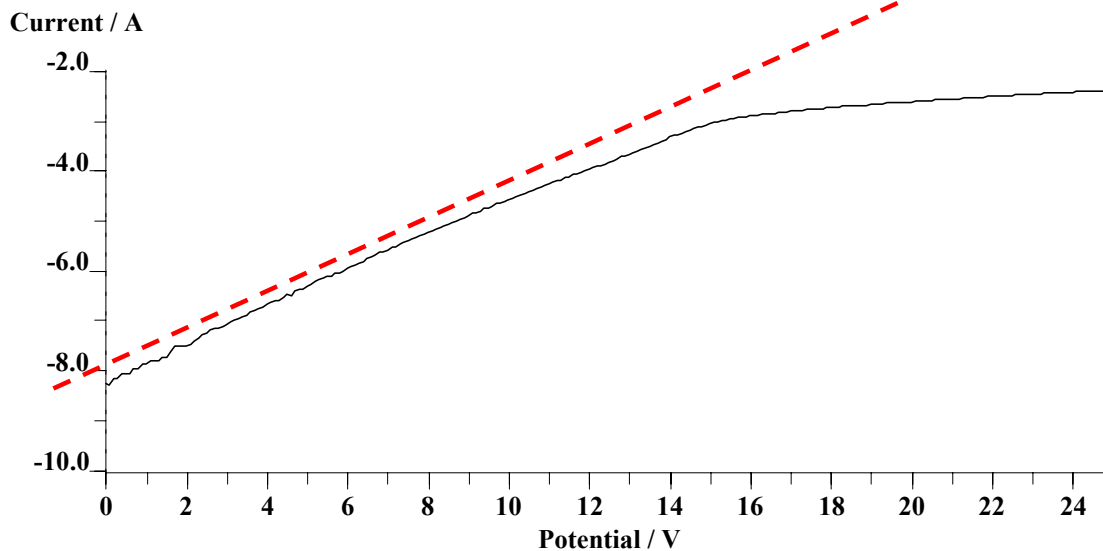


Figure 9: $\ln(I_e)$ vs V_b , with least squares fit line evaluated in the electron retardation region (dashed line); interval is chosen manually by the user. T_e is the reciprocal of the slope: ~ 2.7 eV in this case.

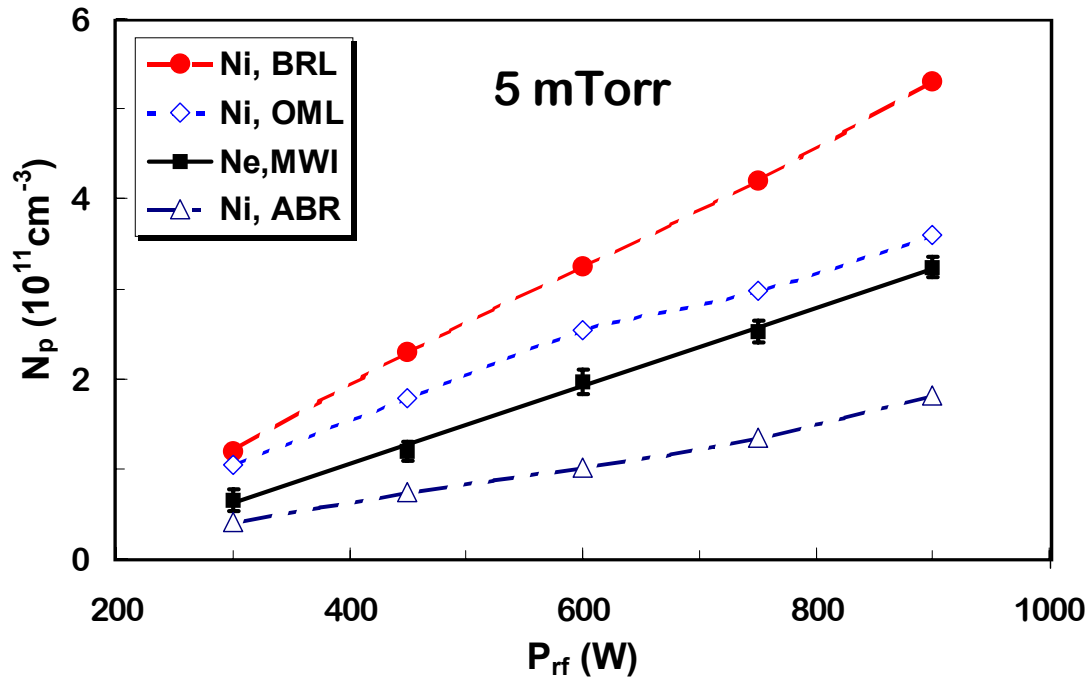


Figure 10. N_p vs P_{rf} , for $P_0 = 5$ mTorr; N_i using BRL, OML and ABR-based algorithms on I - V curves. OML yields the best agreement of the three classical probe theories with the true $N_{e,MWI}$ values.

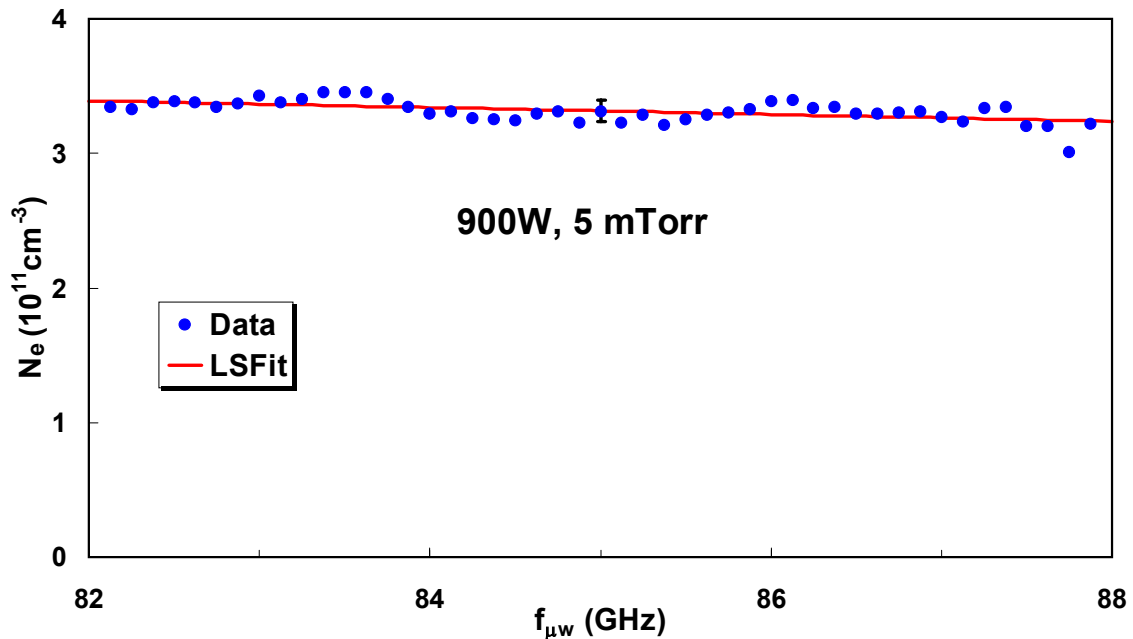


Figure 11: Example of $\langle N_e \rangle_{MWI}$ versus $f_{\mu w}$ over the interval 82-88 GHz, indicating the stability of $\Delta\Phi$ with respect to swept $f_{\mu w}$. Good statistics achieved by sweeping $f_{\mu w}$.

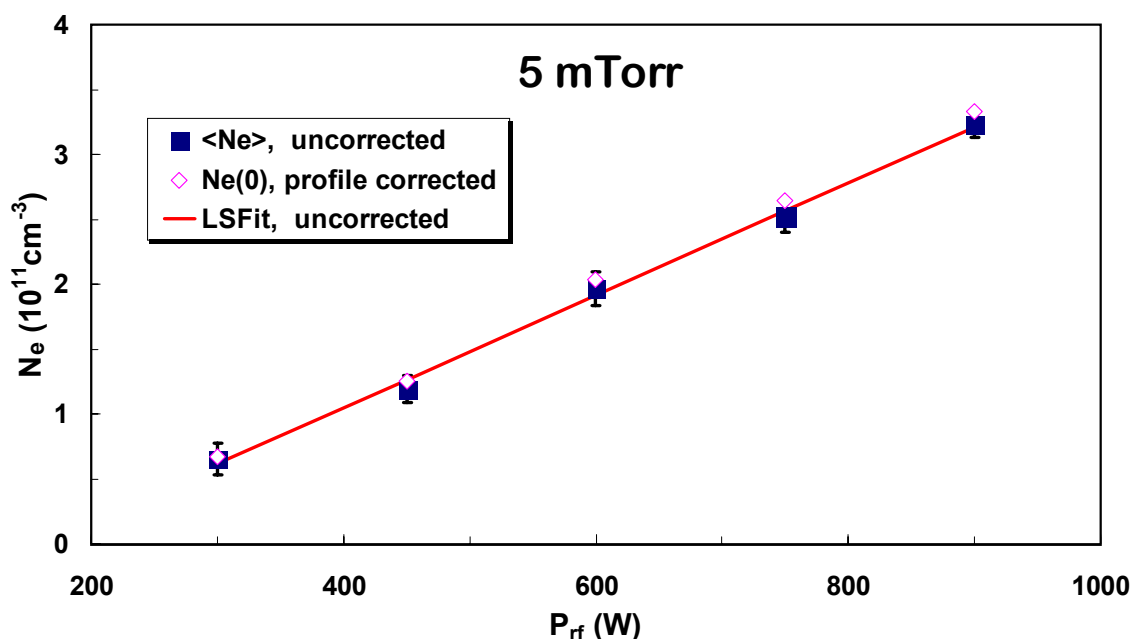


Figure 12: Calibration of $N_e(0)$ from MWI using Abel inversion of $N_i(r)$ from the radially scannable Langmuir probe. "Corrected" $N_e(0)$ and "uncorrected" (Abel inversion not incorporated) $\langle N_e \rangle$ vs P_{rf} . $P_0 = 5 \text{ mTorr}$. Both data sets fall within the error bars; similar results obtained for all P_0 .

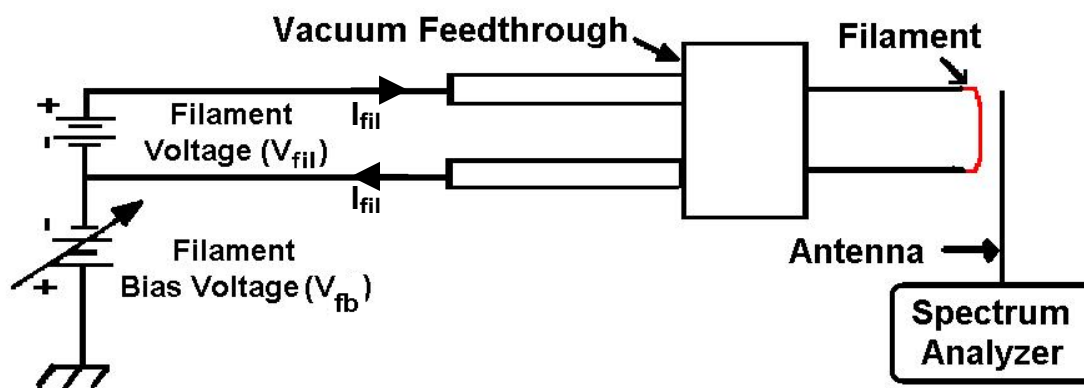


Figure 13: Schematic of POP apparatus, consisting of a filament, an antenna, bias/filament supplies and spectrum analyzer. V_{fb} is applied between probe and chamber to accelerate the electron beam.

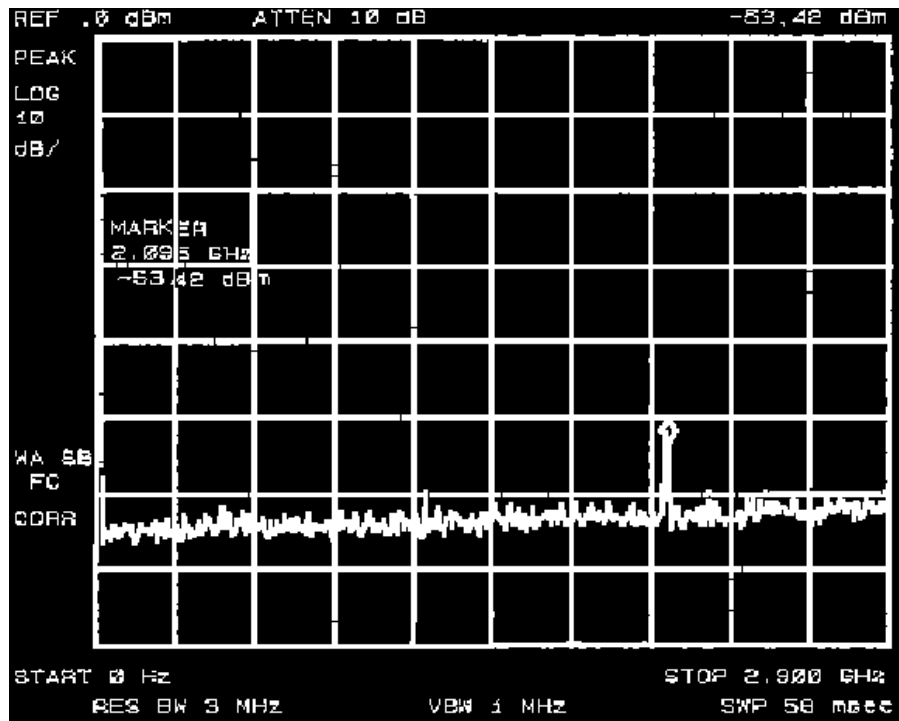


Figure 14: Typical POP signal on spectrum analyzer. Peak at $f_{osc} = 2.095$ GHz yields $N_e = 5.4 \times 10^{10} \text{ cm}^{-3}$. A narrow peak occurs if minimal V_{bf} and I_{fil} are supplied to excite the beam-plasma mode.

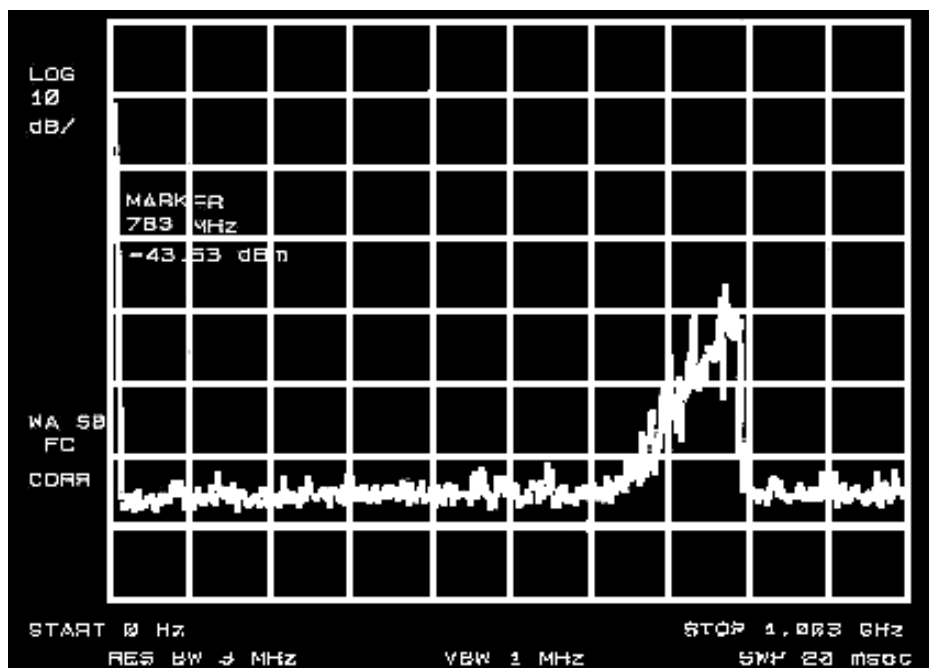


Figure 15: POP spectrum of tenuously localized plasma produced by filament/e-beam only. $P_{rf} = 0$.

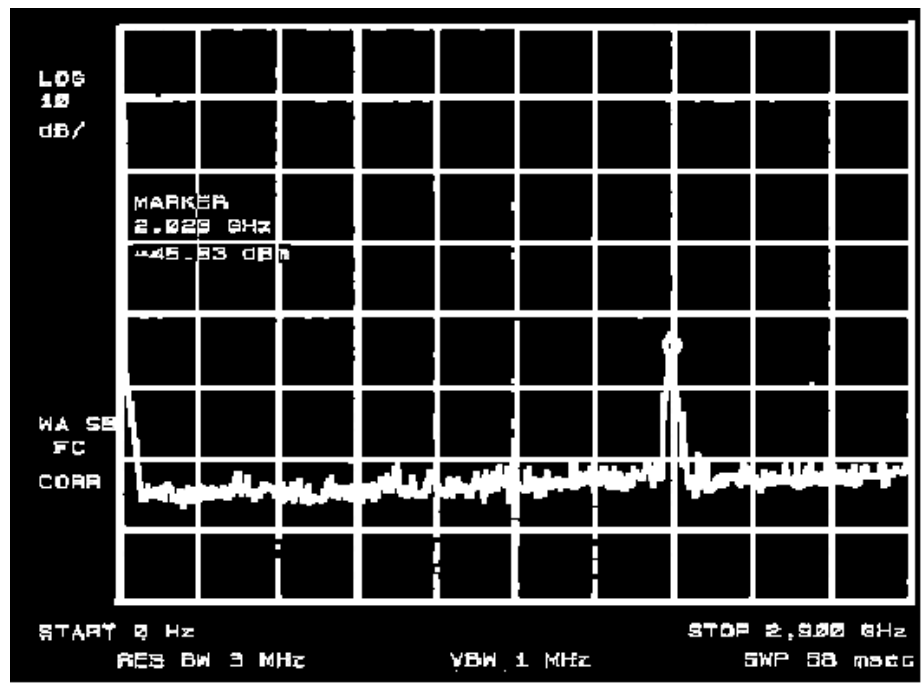


Fig. 16a: Single, but broad, POP peak at $f_{osc} = 2.023\text{GHz}$. Note "skirt" near $f=0$.

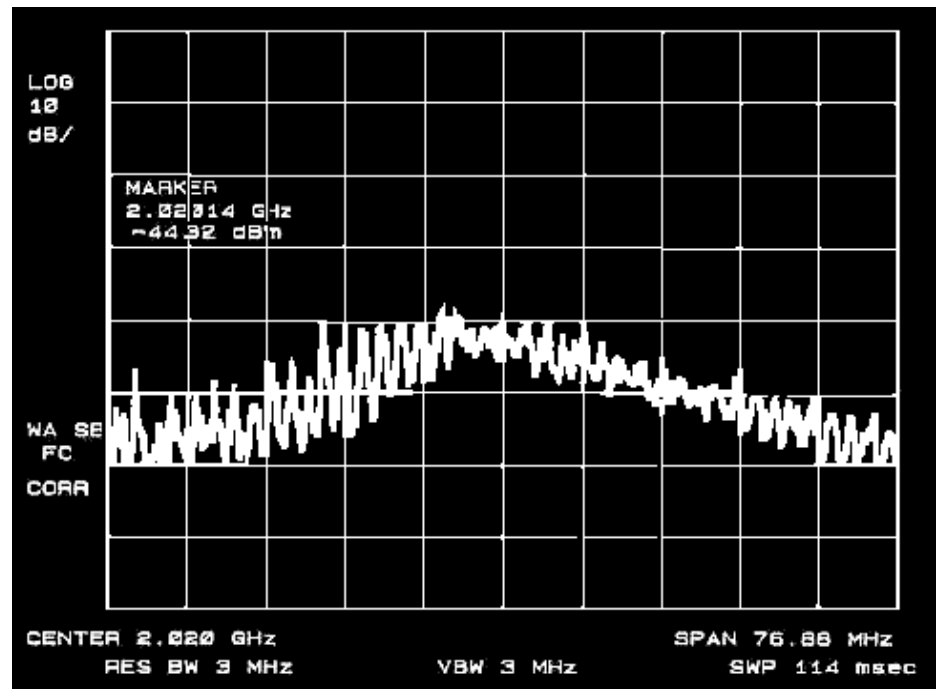


Fig. 16b: Same as (a), but f -scale expanded - sidebands at f_{if} and harmonics observed.

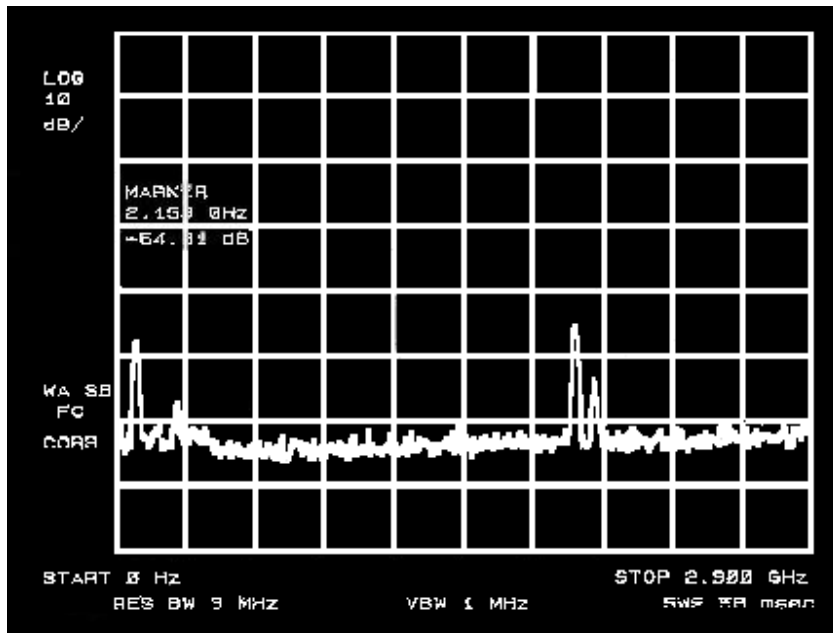


Fig. 17: Two narrow POP peaks centered at ~ 2.1 GHz and ~ 100 MHz apart. Note presence of 100MHz signal and several harmonics as well, possibly due to N_p modulation by RF.

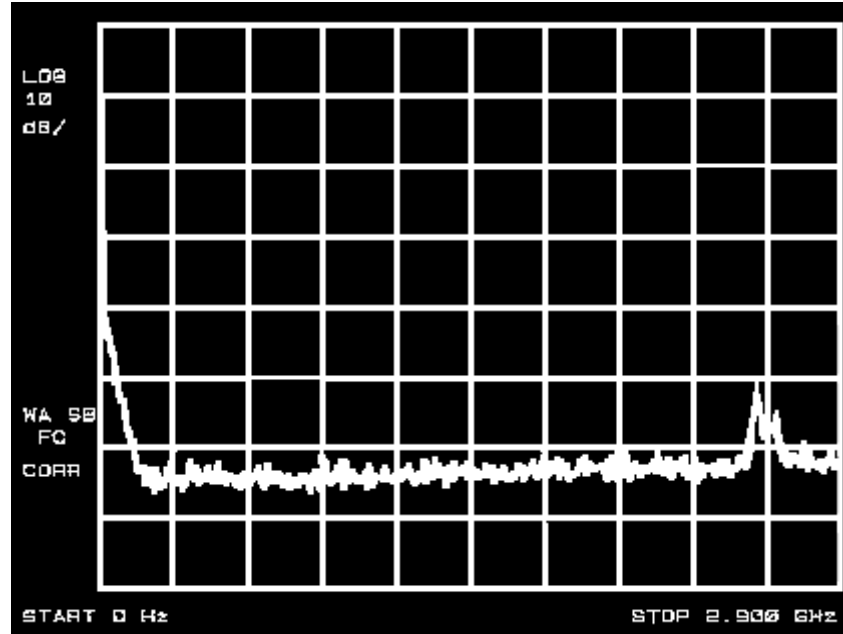


Figure 18: Broad POP split peak due to an overdriven electron beam. $V_{fb} = 230$ V, $I_{fil} = 6.8$ A, more than double the values that yield a single, narrow peak. Broadband skirt near $f = 0$, indicating broadband beating with f_{rf} . $P_0 = 1$ mTorr, $P_{rf} = 450$ W.

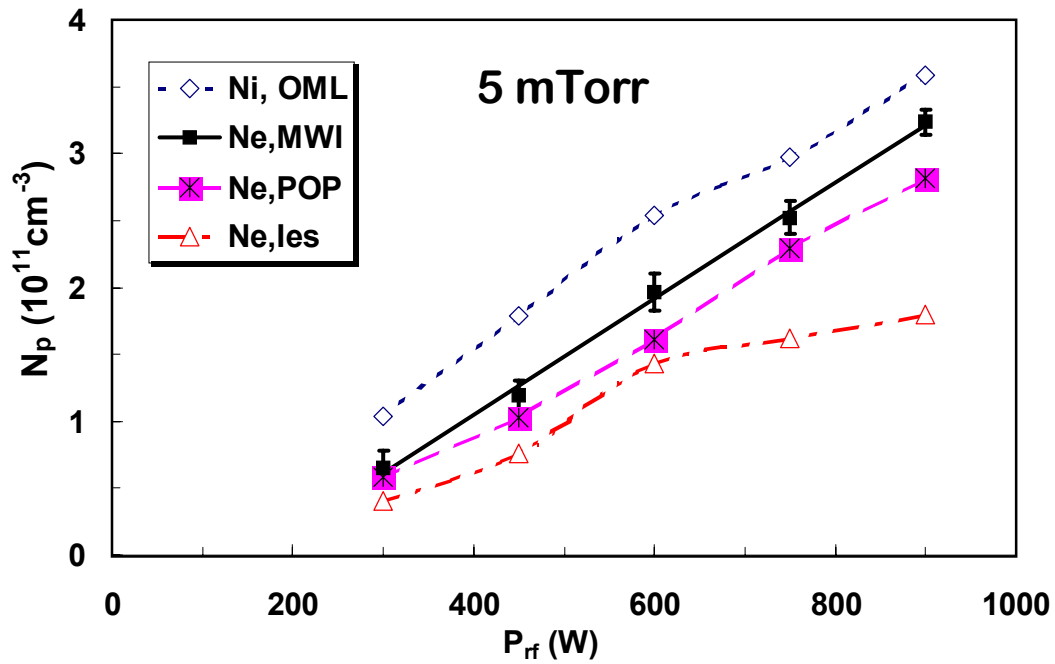


Figure 19a: Same as figure 10, but with $N_{e,POP}$ and $N_{e,les}$ from the Langmuir probe for comparison with $N_{e,MWI}$. $N_{e,les} \leq (N_{e,MWI}, N_{e,POP}) \leq N_{i,OML}$, as previously reported in the literature.

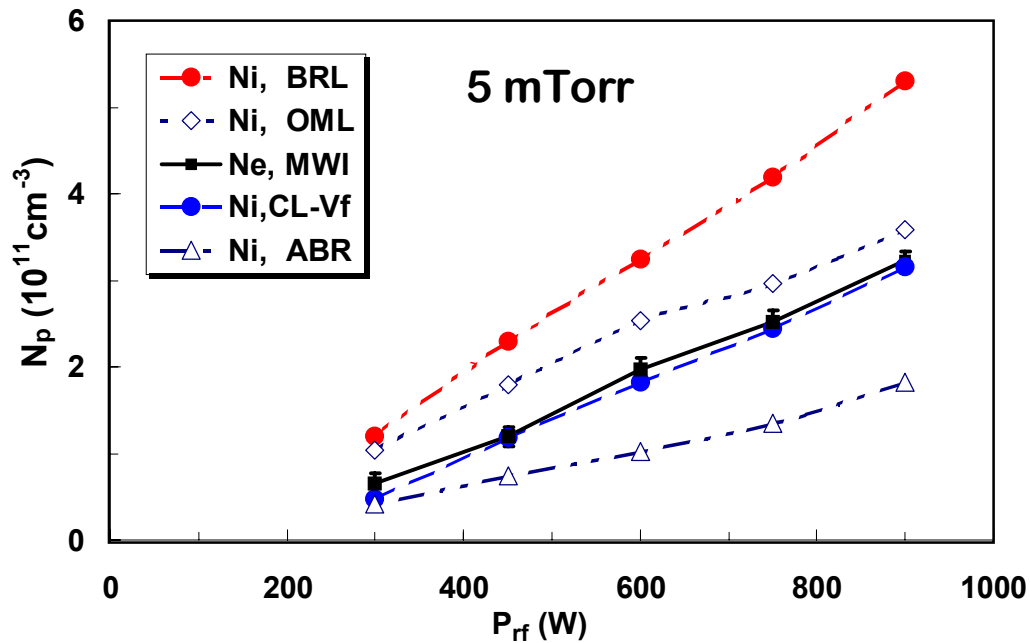


Figure 19b: Same conditions as (a), but just the N_i results from classical Langmuir probe theories and $N_{i,CL-Vf}$ from the Child-Langmuir floating potential approach. $N_{i,CL-Vf}$ yields excellent agreement with $N_{e,MWI}$. BRL represents an upper bound on the theoretical N_i , whereas ABR is the lower bound.

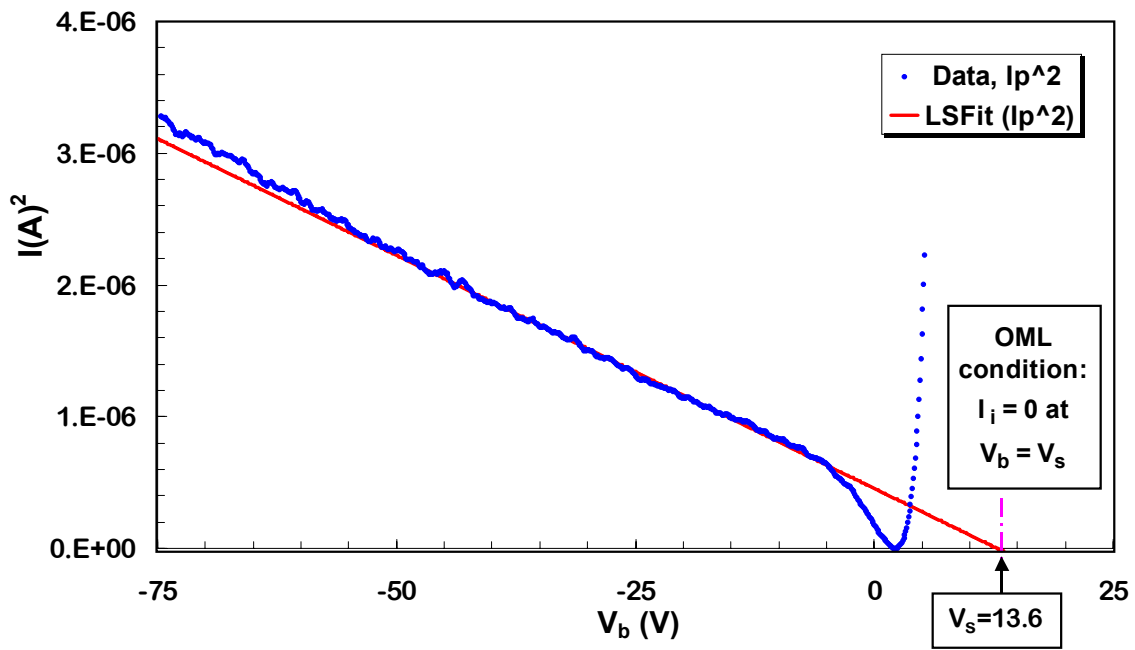


Figure 20a: I^2 vs V_0 fit (solid line) of the I - V curve (dots) obtained for $P_0 = 5$ mTorr, $P_{rf} = 900$ W. Adherence to OML imposes the constraint $I_i \rightarrow 0$ as $V_b \rightarrow V_s \cong 14.2$ V obtained from the 1st derivative.

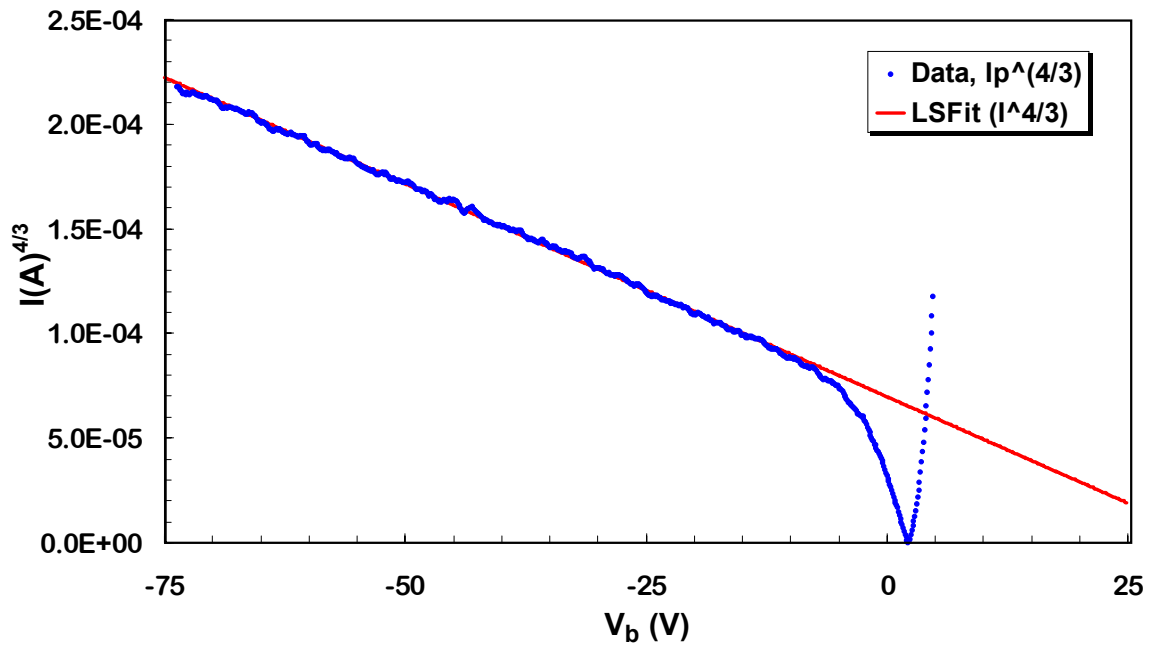


Figure 20b: $I^{4/3}$ vs V_0 fit (solid line) of the same I - V curve (dots) as in (a). Note the high quality of the fit and that no constraint on I_i at the V_b -intercept is imposed.

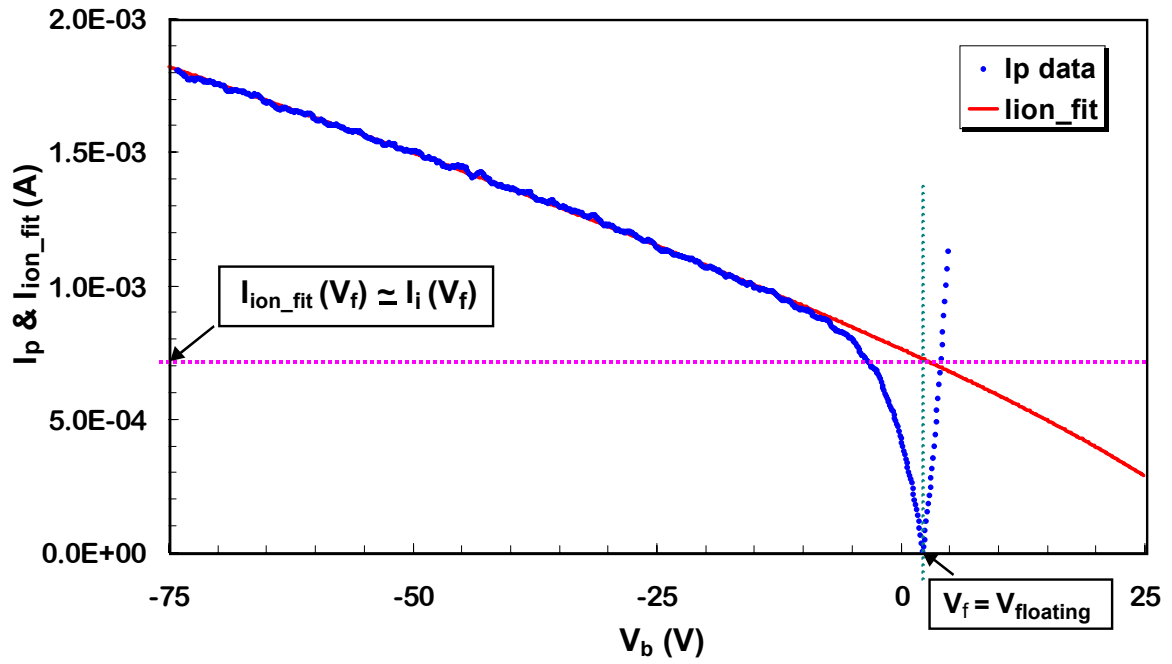


Figure 20c: Inversion of the $I^{4/3} \propto V_0$ fit from (b), plotted as I_{ion_fit} (line) with the I_p data (dots). $I_i(V_f)$ is found by extrapolation of the fit to $V_b = V_f$, and then plugged into equation (3.5) to yield $N_{i,CL-V_f}$.

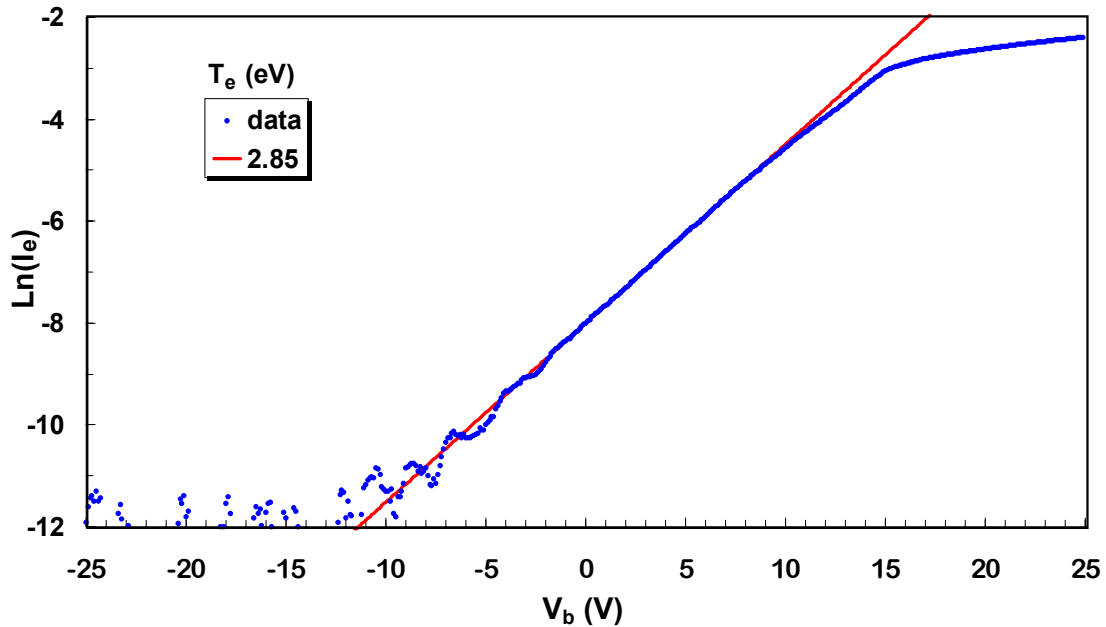


Figure 20d: $\text{Ln}(I_e)$ vs V_b , where $I_e = I_p - I_{ion_fit}$, as calculated from the CL- V_f method. A high quality linear fit is obtained over a fairly wide interval $-7 \text{ V} < V_b < 10 \text{ V}$, yielding $T_e = 2.85 \text{ eV}$.

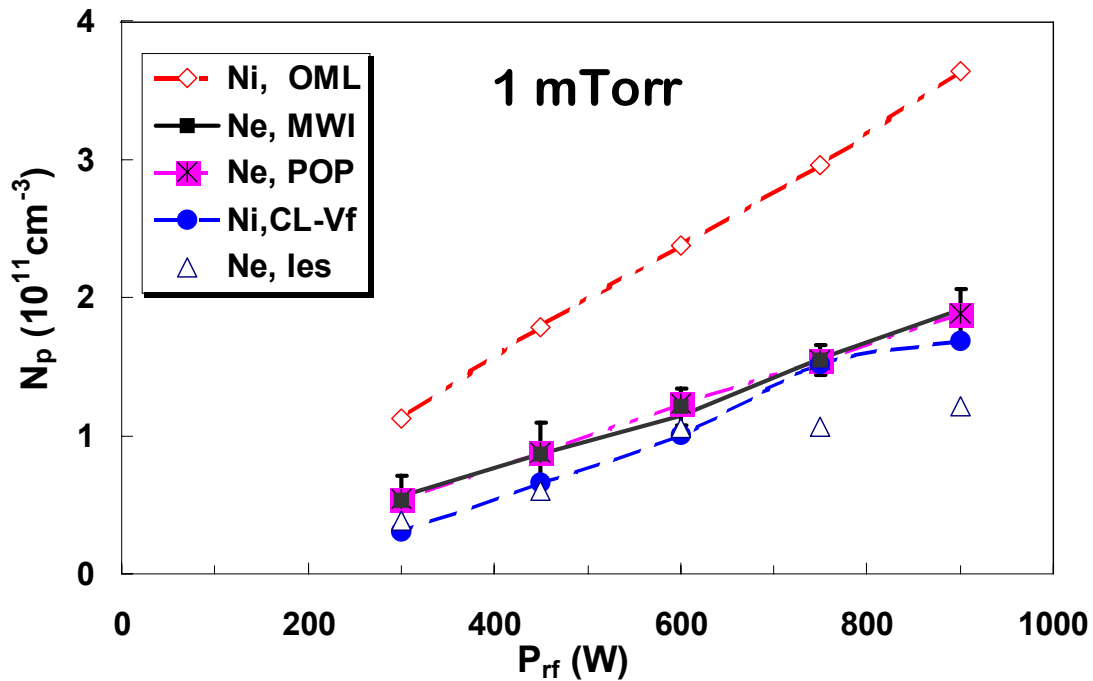


Figure 21a: Comparison of N_p from (a) MWI - $N_{e,MWI}$, (b) POP - $N_{e,POP}$, and the Langmuir probe--the latter using (c) OML - $N_{i,OML}$, (d) the CL- V_f algorithm-- $N_{i,CL-V_f}$, and (e) electron saturation current-- $N_{e,les}$. The ordering $N_{e,les} < (N_{e,POP}, N_{e,MWI}, N_{i,CL-V_f}) < N_{i,OML}$ is observed. Here, $N_{i,POP} \cong N_{e,MWI}$ and $N_{e,MWI} \cong N_{i,CL-V_f} < N_{i,OML}$ at all P_{rf} .

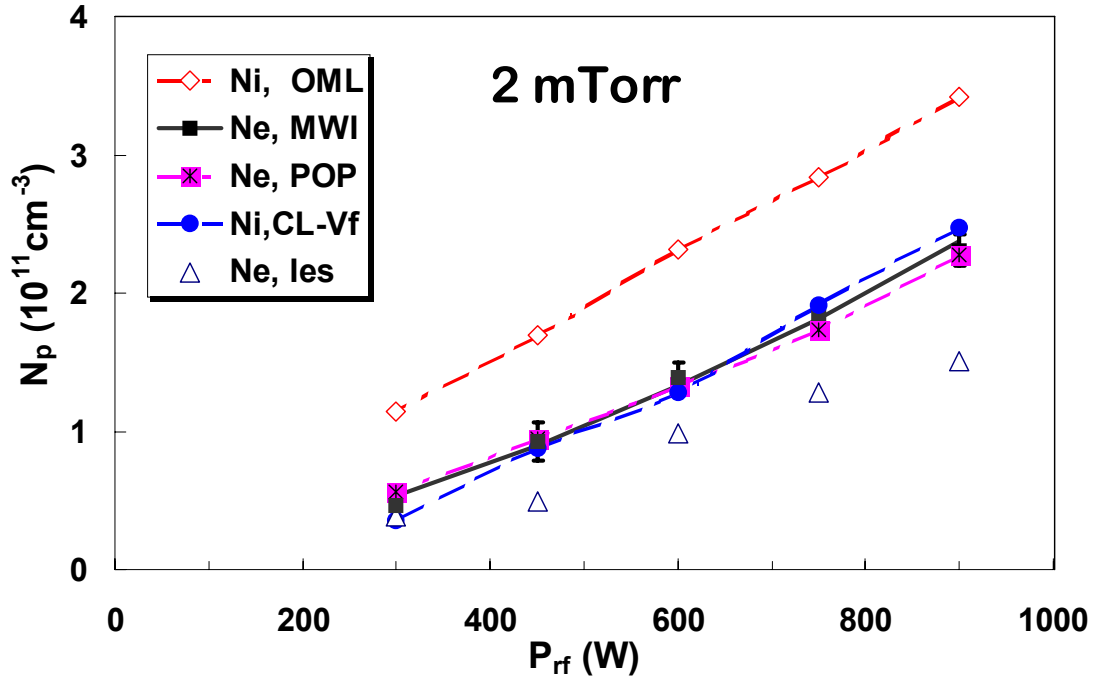


Figure 21b: Same as Figure 21a, but for $P_0 = 2$ mTorr. Same results, except that the success of the CL- V_f approach is more apparent, as is the convergence of the MWI, POP and CL- V_f results.

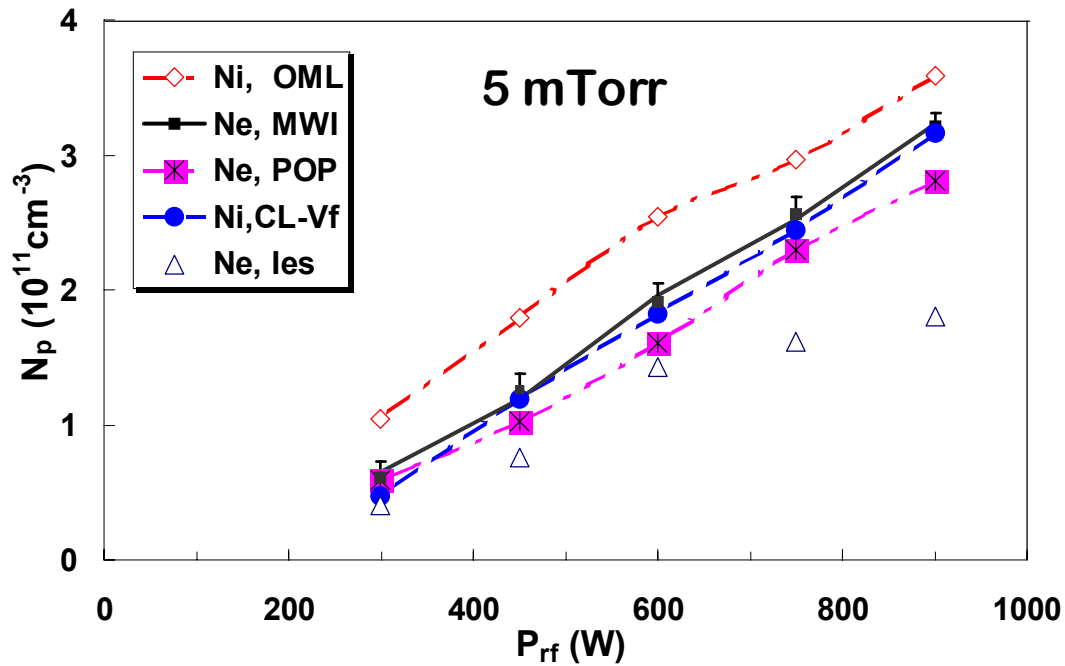


Figure 21c: Same as above, but for $P_0 = 5 \text{ mTorr}$. Note the systematic deviation of $N_{e,POP}$ from the $N_{e,MWI}$ result, and the convergence of the $N_{i,CL-Vf}$ and $N_{e,MWI}$ values, as P_{rf} increases.

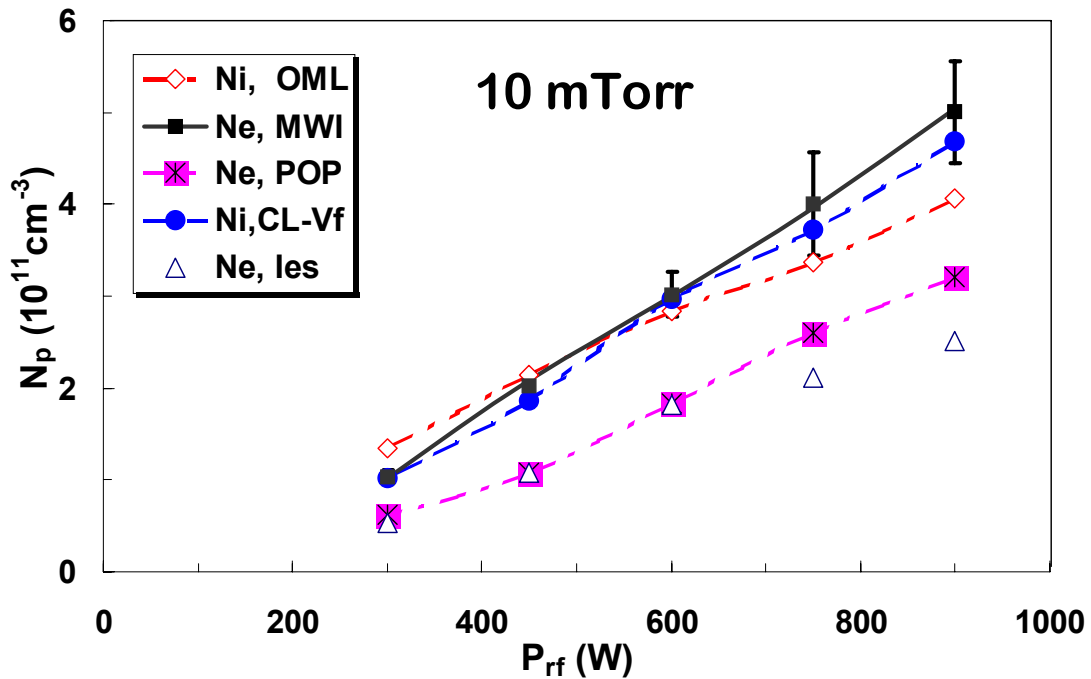


Figure 21d: Same as above, but for $P_0 = 10 \text{ mTorr}$. The ordering $N_{e,les} < N_{e,MWI}$, $N_{e,POP} < N_{i,OML}$ is violated for the first time, for $P_{rf} \geq 600 \text{ W}$. Deviation of $N_{e,POP}$ from $N_{e,MWI}$ increased dramatically from the 5 mTorr case. $N_{i,CL-Vf}$ agrees with $N_{e,MWI}$ to within experimental error in all cases.